

Technical Report, Earth and Space Sciences
No. 8, 2011

Evaluation of a new autofocus algorithm within
the framework of Fast Factorized Back-Projection

Jan Torgrimsson

CHALMERS UNIVERSITY OF TECHNOLOGY
Gothenburg, Sweden, November 2011

Abstract

The following report deals with a new autofocus algorithm within the framework of time domain SAR processing (Fast Factorized Back-Projection). The strategy, developed at SAAB EDS, relies on varying flight track parameters until a sharp image is obtained. Focus measures are provided by a predetermined object function.

After a short introduction and some preliminaries, the algorithm is described in detail, results for two different data sets (collected by the CARABAS II system) are then presented, analyzed and discussed.

The analysis emphasizes some promising attributes. Two of the auto-focused images are for example sharper than corresponding references. It is also shown that two of the variation parameters are separable, this reduces the required number of geometry hypotheses substantially. However, some issues are also raised. A point-like target is for example easily distorted unless the data is upsampled prior to the processing. For the moment, it is not clear if this problem is related to the back-projection or the autofocus algorithm itself. The time consumption is another distinct downside.

The report concludes that a lot of work remains to be done before the algorithm can be considered as functional. A sensitivity study with respect to the variation parameters, as well as a search for alternative object functions should be prioritized. A more conventional autofocus approach is also proposed, to keep options open for the future.

Acknowledgements

P. Dammert

L. Eriksson

H. Hellsten

L. Ulander

A. Åhlander

Index

1	Introduction	5
2	Preliminaries	6
2.1	Frequency domain SAR processing	6
2.2	Time domain SAR processing	6
2.2.1	Global Back-Projection	7
2.2.2	Fast Factorized Back-Projection	8
2.3	Autofocus	11
2.4	CARABAS	12
3	Method	13
3.1	Revision A	16
3.2	The Merging transform	23
3.3	The Range History Preserving transform	29
3.4	Revision B	31
3.5	Preprocessing	37
3.6	Image formation & Object functions	38
3.7	Scenes	39
3.8	Evaluation procedure	39
4	Results - Revision A	44
5	Results - Revision B	52

6	Analysis	60
6.1	Object functions	60
6.2	Images	60
6.3	The trihedral reflector	61
7	Discussion & Conclusions	62
7.1	Present status	62
7.2	Future work	62
8	References	64
I	GBP - Algorithm realization	67
II	FFBP - Algorithm realization	68

1 Introduction

Processing of Synthetic Aperture Radar (SAR) data has traditionally been accomplished by means of frequency domain methods, all assuming a straight flight track at constant altitude. Motion compensation can mitigate minor departures from this ideal assumption. Major departures on the other hand cannot be corrected easily. This fact often degrades the final image [23, 26].

Track requirements¹ are stricter for a wide-beam SAR system and hence, harder to comply with. If not fulfilled, frequency domain processing is a non-ideal approach. Time domain algorithms, i.e. Global Back-Projection (GBP)² [8] and Fast Factorized Back-Projection (FFBP) [23], can handle the challenge, presuming that track parameters are measured accurately.

The performance of an Inertial Measurement Unit (IMU) usually satisfies this purpose. A high precision IMU is however expensive and furthermore export restricted, this leads to a demand to relax the dependence on this device. Autofocus as a supplement to the conventional processing chain is a conceivable solution [5]. Unfortunately, common techniques as MapDrift (MD) [3, 14] and the Phase Gradient Algorithm (PGA) [3, 14] fail to deliver as measurement errors escalate. This deficiency has motivated the development of a new autofocus algorithm at SAAB Electronic Defence Systems (SAAB EDS). In principle, the novel technique varies the track parameters, to find the sharpest image according to some predetermined object function [12].

This report will evaluate two early versions of the algorithm (Revision A and Revision B, see [9] and [10] respectively), through tests on two different data sets, collected by the Coherent All Radio BAnd Sensing (CARABAS) system. In addition three different object functions will be assessed, i.e. correlation, entropy and maximum intensity.

¹Requirements on straightness.

²Referred to as direct- and standard Back-Projection in [23] and [26] respectively.

2 Preliminaries

Before dealing with the proposed autofocus algorithm, some brief background information will be given. It should be emphasized in advance, that a general understanding of SAR processing is expected. Note also that no clear distinction is made between stripmap- and spotlight SAR. This is intentional, as fundamental concepts apply to both modes.

2.1 Frequency domain SAR processing

There are a number of high resolution methods for frequency domain SAR processing. This section will list a selection of well documented techniques. For detailed descriptions, the corresponding references are recommended.

The Polar Format Algorithm (PFA) [3, 14], the Range Doppler Algorithm (RDA) [4] and the Chirp Scaling Algorithm (CSA) [3, 4, 20] can be viewed as basic solutions. These methods introduce many approximations, making it hard to handle challenging system properties. Examples being: wide beamwidth, high squint angle and wide relative bandwidth. Still, if feasible, simplicity and computational efficiency justify the usage.

The Extended Chirp Scaling Algorithm (ECSA) [17], the Range Migration- or ΩK Algorithm (RMA/ ΩKA) [2–4] and Fourier-Hankel inversion [1, 7, 11] can be viewed as sophisticated solutions. These methods introduce fewer approximations, making it possible to cope with the mentioned properties.

2.2 Time domain SAR processing

GBP and FFBP are high resolution methods for time domain SAR processing. Thus far, utilization of the first approach has been restricted due to the large number of computations required to form an image. The quite recently developed factorized approach reduces the required number of computations substantially, without affecting image quality appreciably. FFBP actually makes it possible to process SAR data efficiently in the time domain, providing a complement to conventional frequency domain methods [23].

To fully understand the new autofocus algorithm, it is important to first be familiar with the principles behind GBP and FFBP. The upcoming subsections will therefore be dedicated to an overview of these methods.

2.2.1 Global Back-Projection

As the name implies, GBP back-projects range compressed radar echoes to pixel positions in an arbitrarily chosen Image Display Plane (IDP). This is done for all transmit-/receive locations along the flight track. From now on, these locations will also be referred to as stationary positions, reflecting the adopted start-/stop approximation.

A complex data vector is attained at each track position. Every address or bin is associated with a certain range. Convolution of the vector with a matched filter gives the range compressed result³ [4, 22]. After choosing an area to image, i.e. an anchor point, a display angle, a number of pixels and a 2-dimensional pixel spacing, the processing can begin⁴.

Each stationary position contributes with a data value to each pixel in the image. Complex values are added coherently, causing constructive and destructive interference. The image formation can in consequence be regarded as a coherent summation of low resolution sub-images [16, 23, 26].

The slant range between a specific track position and pixel determines which data value to accumulate. As a value coinciding with the calculated range usually cannot be found among available samples, interpolation applies. For demodulated data, each interpolated value must in addition be multiplied by a phase factor. This is not necessary if the data includes the carrier [23, 26].

A well-known flight track following a non-straight path does not pose a problem, as the track is taken into account when calculating the correct range. Topography variations can in turn be compensated for by means of a Digital Elevation Model (DEM). This is not possible to the same extent when working in the frequency domain [23, 26].

Equations for a basic GBP realization are available in Appendix I.

³In practice, fast convolution in the frequency domain performs the compression [4, 22].

⁴The following description of GBP omits a scaling operation and a ramp filter, not essential for understanding the principles. See [23] for further information.

2.2.2 Fast Factorized Back-Projection

The number of computations associated with GBP is proportional to the number of stationary positions times the total number of pixels. For long tracks and large images, the processing time becomes a bottleneck [16, 23, 26]. FFBP reduces the number of computations by reducing the number of stationary positions. The factorization can be accomplished in various ways. This section will describe one possible procedure [23, 24], relevant in context of the proposed autofocus algorithm.

Consider an airborne platform, conveying a wide-beam SAR system with an integration angle of 70 degrees. To simplify the discussion, the platform travels along a straight flight track at constant altitude, the ground below is furthermore assumed flat. This basically implies that from a focusing perspective, the 3-dimensional geometry is reduced to a 2-dimensional geometry. In other words, the elevation angle does not affect image focus⁵ [23, 24].

At equidistant⁶ transmit-/receive locations, the antenna pattern illuminates an extensive area. The radiation is reflected and as before, complex data vectors are attained. The overlap of the pattern between adjacent locations gives very similar concentric range circles within limited sectors. This makes it possible to combine samples from adjoining vectors [23, 24].

In principle, two range compressed data vectors or two physical aperture lobes (70 degrees), can be merged to form a synthetic sub-aperture, emitting two sub-lobes (two updated data vectors) with twice as fine angular resolving capability (35 degrees). The sub-lobes emanate in different directions from a centre found in between original locations. Hence, the number of positions is reduced by a factor two. In the next factorization step, the sub-apertures are merged two and two (see Figure 1), leading to finer resolving capability (four sub-lobes→17.5 degrees) and even fewer positions (reduced by a factor four).

The factorization is repeated time after time until one single stationary position remains⁷. At this point, the image formation described in the previous section applies, now with interpolation in angle as well as range.

⁵Note that this statement also holds for a non-flat ground, this due to the cylindrical symmetry of a straight flight track. See [23] for further information.

⁶This is not a strict requirement for time domain algorithms.

⁷The number of original data vectors determines if this is feasible. In the example, the number would have to be a power of two.

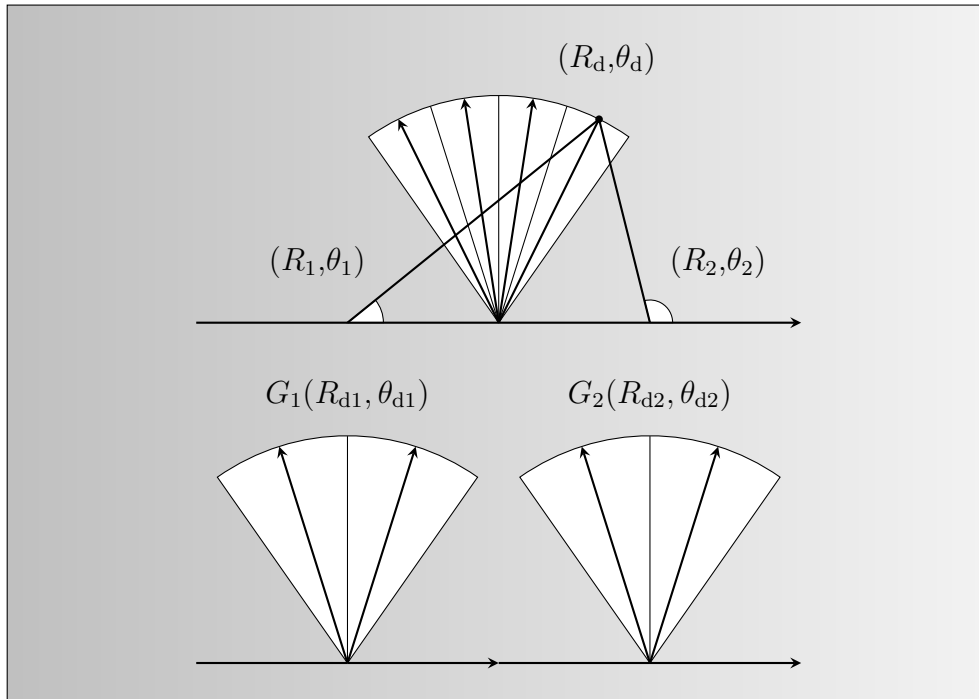


Figure 1 (Top) shows how to find an updated data value for a certain slant range (R_d) and sub-lobe angle (θ_d). First, range (R_1/R_2) and angle (θ_1/θ_2) from preceding sub-aperture centres are calculated. (Bottom) Interpolation of prior sub-lobes ($G_1(R_{d1}, \theta_{d1})$ and $G_2(R_{d2}, \theta_{d2})$ respectively) then gives the corresponding contributions. After multiplying these by phase factors, a coherent addition produces the desired value. It should be pointed out, that the purpose of this figure is to demonstrate the principle. Obviously in this case, no overlap occurs. See also [23, 24].

An alternative is to regard the factorized result as the image, given in polar coordinates, i.e. slant range vs. sub-lobe angle. If the factorization is terminated in advance, additional positions will be left. This will result in a less approximate but also less efficient realization, as FFBP closes in on GBP.

In general, the base for both the aperture- and the lobe factorization can be chosen freely. Note though, that the choices will affect image quality as well as processing time. Oversampling sub-lobes will for example be very time consuming⁸. The end result may however be a valid motivation.

⁸Instead of oversampling sub-lobes, angular interpolation with cubic kernels may be put into practice (a nearest neighbour interpolation approach is normally employed). See [8] for further information.

If a nonlinear track is covered by the platform (still assuming flat ground), the geometry cannot be reduced. The elevation angle now affects image focus, meaning that points from where the radar echoes were reflected must be located. Naturally this complicates the factorization [23, 24].

The flight track is synthesized as a piecewise linear path, possible as each stationary position possess a direction vector. This way of visualizing the sub-apertures is recurrent in upcoming discussions [12].

New sub-aperture centres⁹ are in addition found between adjacent preceding centres or alternatively between the beginning of one preceding vector and the end of the other. The latter option is presumed from now on [12].

Equations for a basic FFBP realization are available in Appendix II.

⁹New sub-aperture centres → New stationary positions.

2.3 Autofocus

In the context of SAR processing, autofocus is the use of information in the defocused image to estimate and correct phase errors [3, 22]. Standard techniques are 1-dimensional and apply equally well in range and azimuth. However, phase errors in azimuth are in practice more critical¹⁰ [3].

MD and the PGA are examples of extensively used autofocus techniques. A common course of action is to employ the model-based MD method to pull-in¹¹ a dominant quadratic error component. The PGA may then act as a capable complement by removing higher order components as well.

Other autofocus techniques mentioned in the literature are: Multiple Aperture MapDrift (MAMD) [3] and the Phase Difference Algorithm (PDA) [3]. Additionally, various procedures based on entropy minimization/contrast maximization are suggested. See [15, 18, 25, 27] for further information.

The convention is to postulate that azimuth phase errors reside in separate range bins, meaning that after focusing the data deterministically, there should be no residual Range Cell Migration (RCM) due to measurement errors. Furthermore, space invariance is presumed, implying that properties of erroneous phase components should be independent of range [3, 6].

For a high resolution, wide-beam SAR system, these criteria may not be satisfied. This leads to a call for sophisticated solutions [6, 12].

Autofocusing partial images individually is a computationally demanding approach for dealing with space variant phase errors [3]. Innovative algorithms mitigating residual RCM have also been reported and show promising results [6], but have not been widely accepted yet.

In addition it should be stressed, that Prominent Point Processing (PPP) can compensate for phase errors without introducing either of the restrictions above. The technique is however not automatic and furthermore relies on the existence of strong point-like targets¹² [3].

The proposed autofocus algorithm has the potential to handle both residual RCM and space variant effects for a scene of arbitrary structure [12].

¹⁰Phase errors on account of the transmitter/receiver, are normally small [3].

¹¹To pull-in \rightarrow To resolve 2π ambiguities associated with large phase errors.

¹²The existence of point-like targets is a general presumption in the field of autofocus [3].

2.4 CARABAS

CARABAS is a VHF (Very High Frequency) SAR system operating between $\sim 20\text{--}90$ MHz, giving a bandwidth of ~ 70 MHz and a centre frequency of ~ 55 MHz. The low frequencies penetrate foliage, making it possible to detect hidden targets, an important aspect of military ground surveillance. Applications in forestry may also benefit from this feature.

The first CARABAS system was developed during the 80's at the Swedish Defence Research Establishment (FOA)¹³. Later, Ericsson Microwave Systems (EMW)¹⁴ joined the project as well. The development is still ongoing, with a third CARABAS system currently being put to the test.

Note that the data sets dealt with in this report have been acquired by the CARABAS II system (broadside stripmap mode). See [13] for further information. Also note that an upgraded variant of the new autofocus algorithm, which now will be described, is to be incorporated with future systems.



Figure 2 shows a drawing of an aircraft carrying the distinctive CARABAS antennae configuration. Credit SAAB EDS.

¹³Since 2001, the Swedish Defence Research Agency (FOI).

¹⁴Later SAAB Microwave Systems (SMW) and at present SAAB EDS.

3 Method

Consider the following scenario; complex data vectors are attained along a nonlinear track, the ground is still assumed flat. After compression, the echoes are factorized until two stationary positions remain. Despite measurement errors, the (polar) sub-images are focused, this due to limited angular resolution. In preparation for the final factorization step, the flight track is once again synthesized as a piecewise linear path. Denote the start point Q_{01} , the cut-off point Q_{02} and the end point Q_{03} (see Figure 3).

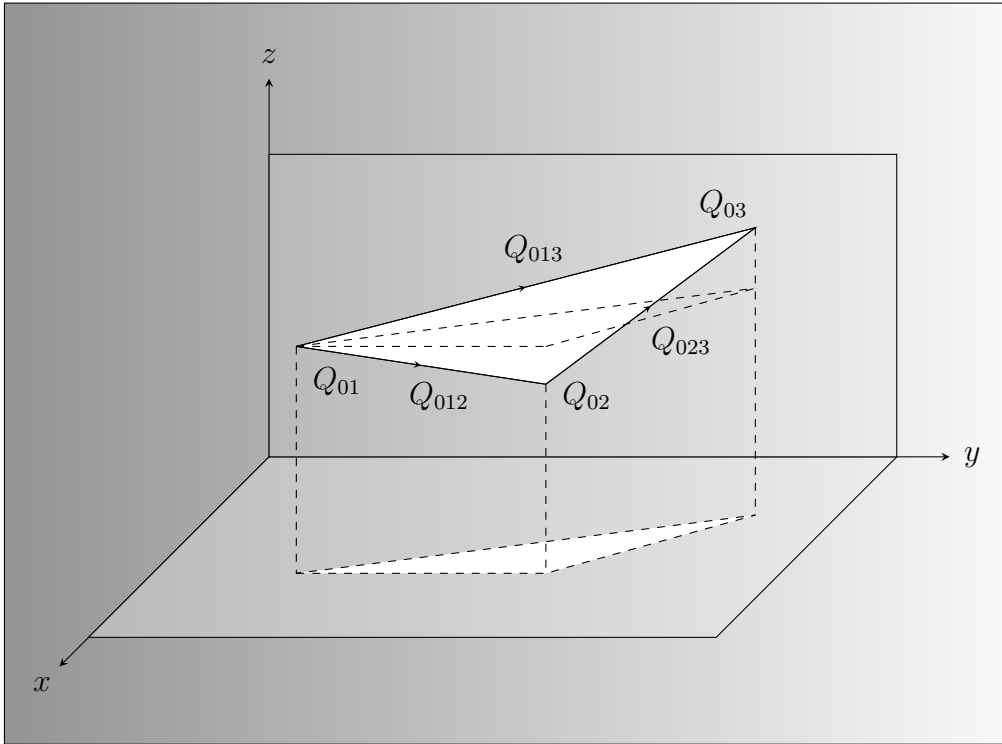


Figure 3 shows the geometry of the sub-aperture triangle. The flight track is along the y -axis (nominally) in a right handed Cartesian coordinate system (z -axis defined positive). This arrangement is presumed throughout the report. The travel time for Q_{013} is $2T$, while the travel time for Q_{012}/Q_{023} is T .

After the factorization, the resulting polar image is defocused. This indicates that the sub-aperture triangle formed by Q_{01} , Q_{02} and Q_{03} is incorrect. If allowed to place the points anywhere in three dimensions, an arbitrary triangle can be formed, obviously including the correct one.

Presume now that images for all practical tracks are produced and marked with a focus measure. The image with the best measure may then be treated as the true image. This is the main idea of the autofocus algorithm, possible to realize in discrete form and easily integrated.

The processing time is however bound to be extensive, especially if the algorithm is supposed to support early factorization steps as well. Fortunately, under some premises, there is no need to reprocess from scratch. It is shown in [9, 10, 12], that different geometry hypotheses may be evaluated through two transforms: one Merging¹⁵ (M) and one Range History Preserving (RHP). Updated images are then found by interpolating the last focused sub-image pair onto polar grids and adding these coherently.

From now on the final image and the sub-images are assumed to be ground projected. In other words, the algorithm works in the xy-plane, with ground ranges and ground sub-lobe angles [9, 10, 12].

The projection procedure can be considered as preprocessing and is described in sub-section 3.5. Note that terms like image(s), range(s) and angle(s) now are associated with the xy-plane exclusively.

The variation of the track should be confined to a number of independent parameters (the fewer the better). Before choosing these (see sub-section 3.1 and 3.4), it is important to isolate what actually affects image focus.

First it should be stressed, that while varying the geometry, path segments (Q_{012}/Q_{023}) remain connected. Thus the triangle may be modeled by:

- The position of the cut-off point.
- The angular orientations of the segments.
- The speeds (the lengths) of the segments.

A measurement error regarding the position of the cut-off point in the horizontal plane, will translate the final image.

An erroneous altitude will in turn offset the Focus Target Plane (FTP) vertically, defocusing the image if the Height Of Focus (HOF) is insufficient.

¹⁵Referred to as a Ground reflectivity preserving (G) transform in [9, 10, 12].

A measurement error regarding the angular orientation of the triangle, will if restricted to the horizontal plane rotate the final image.

If not, the FTP will be tilted, defocusing the image if the HOF is insufficient.

In Revision A and B it is presumed that the HOF is satisfying, making it possible to fix the position and orientation of one segment (including \mathbf{Q}_{013}).

The last few paragraphs indicate that the geometry may be modified by means of two angles and two speeds, all in all four independent parameters.

If the HOF is insufficient, it is not possible to fix one segment and hence, two additional parameters must be taken into account: one introducing an overall altitude alteration and one tilting the triangle vertically.

It is stated in [9, 10, 12], that translations and rotations in the xy-plane do not affect focus of the sub-image contributions.

These variations are assessed with the M-transform [9, 10, 12].

It is also stated, that vertical tilts and altitude alterations do not affect focus of the sub-image contributions. Geometric distortions are however introduced. Changing the speeds of the segments ($\mathbf{Q}_{012}/\mathbf{Q}_{023}$) will in addition both distort and defocus contributing images.

These variations¹⁶ are assessed with the RHP-transform [9, 10, 12].

This concludes the overview of the algorithm, the details will now be discussed concisely. Note in advance that sub-section 3.1 and 3.4 compile equations found in [9] and [10] respectively (and additional equations as well).

These sub-sections are intentionally short, but should be comprehensible once the basics of Revision A and B are clear.

¹⁶Small non-defocusing speed alterations are considered in this context.

3.1 Revision A

In Revision A [9], Q_{12} (with Q_{012} as a special case) is presumed to be parallel to the xy -plane at all times. Hence, an interpolation routine must modify focused sub-image pairs in agreement with necessary geometry changes. If the algorithm is applied at the final factorization step, the routine¹⁷ may be implemented prior to the ground projection (in the slant plane).

The assumed geometry is established in the figure below, while the upcoming table enumerates all significant parameters.

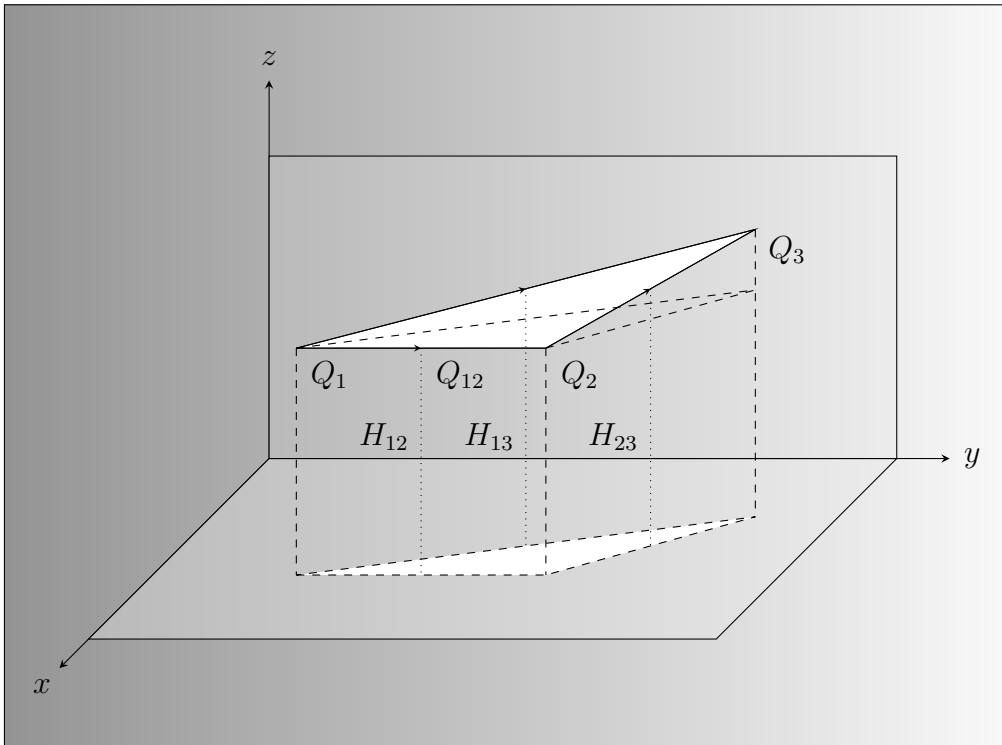


Figure 4 shows the Rev. A geometry, all vectors are not denoted, but understood from Figure 3. Notice that Q_{12} is parallel to the horizontal plane, also note that altitudes are marked out for clarification.

¹⁷Since this interpolation routine is very similar to the one described in section 3.5, it will not be discussed further in this report.

Table 1 resumes the notations of Rev. A parameters, short descriptions and some comments are also tabulated. Table 1 continues on the next page.

Notation	Description	Comment
Q_{01}, Q_{02}, Q_{03}	Start-, cut-off- and end point of flight track (x,y,z) (m).	Constant quantities, given, navigation parameters.
$Q_{p01}, Q_{p02}, Q_{p03}$	Projected points (x,y) (m).	Constant quantities, given.
$Q_{012}, Q_{023}, Q_{013}$	Initial direction vectors (x,y,z) (m).	Constant quantities, derived.
$Q_{p012}, Q_{p023}, Q_{p013}$	Projected vectors (x,y) (m).	Constant quantities, derived.
Q_{12}, Q_{23}, Q_{13}	Updated direction vectors (x,y,z) (m).	Varying quantities, not derived.
$Q_{p12}, Q_{p23}, Q_{p13}$	Projected vectors (x,y) (m).	Varying quantities, not derived.
$H_{012}, H_{023}, H_{013}$	Initial altitudes (midpoints) (m).	Constant quantities, derived.
H_{12}, H_{23}, H_{13}	Updated altitudes (midpoints) (m).	Varying quantities, derived.
PRF	Pulse Repetition Frequency (Hz).	Constant quantity, given.
N	Number of pulses for one sub-aperture.	Constant quantity, given.
T	Travel time for one sub-aperture (s).	Constant quantity, derived.
$V_{012}, V_{023}, V_{013}$	Initial speeds (m/s).	Constant quantities, derived.
V_{12}, V_{23}	Updated speeds (m/s).	Variation quantities, user-defined values.
V_{13}	Updated speed (m/s).	Varying quantity, derived.
V_{p012}, V_{p023}	Initial horizontal speeds (m/s).	Constant quantities, derived.
V_{p12}, V_{p23}	Updated horizontal speeds (m/s).	Varying quantities, derived.
V_{z012}, V_{z023}	Initial vertical velocities (signed) (m/s).	Constant quantities, derived.

Notation	Description	Comment
V_{z12}, V_{z23}	Updated vertical velocities (signed) (m/s).	Varying quantities, derived.
χ_0	Angle between Q_{012} and Q_{023} (rad).	Constant quantity, derived.
χ_{p0}	Angle between Q_{p012} and Q_{p023} (rad).	Constant quantity, derived.
χ_{z0}	Angle between Q_{023} and Q_{p023} (rad).	Constant quantity, derived.
χ	Angle between Q_{12} and Q_{23} (rad).	Varying quantity, derived.
χ_p	Angle between Q_{p12} and Q_{p23} (rad).	Varying quantity, derived.
χ_z	Angle between Q_{23} and Q_{p23} (rad).	Varying quantity, derived.
ζ_0	Angle between Q_{012} and Q_{013} (rad).	Constant quantity, derived.
ζ_{p0}	Angle between Q_{p012} and Q_{p013} (rad).	Constant quantity, derived.
ζ_{z0}	Angle between Q_{013} and Q_{p013} (rad).	Constant quantity, derived.
ζ	Angle between Q_{12} and Q_{13} (rad).	Varying quantity, derived.
ζ_p	Angle between Q_{p12} and Q_{p13} (rad).	Variation quantity, user-defined values.
ζ_z	Angle between Q_{13} and Q_{p13} (rad).	Variation quantity, user-defined values.
$R_{d12}, R_{d23}, R_{d13}$	Ground ranges (discrete values) (m).	Constant quantities, see section 3.5.
$\Phi_{d12}, \Phi_{d23}, \Phi_{d13}$	Ground sub-lobe angles (discrete values) (rad).	Constant quantities, see section 3.5.
R_{M12}, R_{M23}	M-transformed ground ranges (m).	Varying quantities, derived, section 3.2.
Φ_{M12}, Φ_{M23}	M-transformed ground sub-lobe angles (rad).	Varying quantities, derived, section 3.2.
R'_{M12}, R'_{M23}	M- and RHP-transformed ground ranges (m).	Varying quantities, derived, section 3.3.
Φ'_{M12}, Φ'_{M23}	M- and RHP-transformed ground sub-lobe angles (rad).	Varying quantities, derived, section 3.3.

In Table 1, angles denoted by the Greek letter Φ are defined between 0 and π , all other angles are defined between $-\pi/2$ and $\pi/2$. A subscript zero indicates an initial state, while a p stands for projected. Quantities will now be derived by means of given system-/track parameters and user-defined variables.

$$Q_{012} = Q_{02} - Q_{01} \quad (1)$$

$$Q_{023} = Q_{03} - Q_{02} \quad (2)$$

$$Q_{013} = Q_{03} - Q_{01} \quad (3)$$

$$Q_{p012} = Q_{p02} - Q_{p01} \quad (4)$$

$$Q_{p023} = Q_{p03} - Q_{p02} \quad (5)$$

$$Q_{p013} = Q_{p03} - Q_{p01} \quad (6)$$

$$H_{012} = (Q_{01_z} + Q_{02_z})/2 \quad (7)$$

$$H_{12} = H_{012} \quad (8)$$

$$H_{023} = \frac{V_{023}T}{2} \cdot \sin \chi_{z0} + H_{012} \quad (9)$$

$$H_{23} = \frac{V_{23}T}{2} \cdot \sin \chi_z + H_{12} \quad (10)$$

$$H_{013} = V_{013}T \cdot \sin \zeta_{z0} + H_{012} \quad (11)$$

$$H_{13} = V_{13}T \cdot \sin \zeta_z + H_{12} \quad (12)$$

$$T = N/PRF \quad (13)$$

$$V_{012} = \|\mathbf{Q}_{012}\|/T \quad (14)$$

$$V_{023} = \|\mathbf{Q}_{023}\|/T \quad (15)$$

$$V_{013} = \|\mathbf{Q}_{013}\|/2T \quad (16)$$

$$V_{13} = \frac{1}{2} \cdot \sqrt{V_{12}^2 + V_{23}^2 + 2V_{12}V_{23} \cos \chi} \quad (17)$$

$$V_{p012} = \sqrt{(V_{012}^2 - V_{z012}^2)} \quad (18)$$

$$V_{p023} = \sqrt{(V_{023}^2 - V_{z023}^2)} \quad (19)$$

$$V_{p12} = \sqrt{(V_{12}^2 - V_{z12}^2)} \quad (20)$$

$$V_{p23} = \sqrt{(V_{23}^2 - V_{z23}^2)} \quad (21)$$

$$V_{z012} = 0 \quad (22)$$

$$V_{z023} = V_{023} \cdot \sin \chi_{z0} \quad (23)$$

$$V_{z12} = 0 \quad (24)$$

$$V_{z23} = V_{23} \cdot \sin \chi_z \quad (25)$$

$$\pm \cos \zeta_0 = \frac{\mathbf{Q}_{012} \cdot \mathbf{Q}_{013}}{\|\mathbf{Q}_{012}\| \cdot \|\mathbf{Q}_{013}\|} \quad (26)$$

$$\pm \cos \zeta = \cos \zeta_p \cos \zeta_z \quad (27)$$

$$\pm \cos \zeta_{p0} = \frac{\mathbf{Q}_{p012} \cdot \mathbf{Q}_{p013}}{\|\mathbf{Q}_{p012}\| \cdot \|\mathbf{Q}_{p013}\|} \quad (28)$$

$$\pm \cos \zeta_{z0} = \frac{\mathbf{Q}_{013} \cdot \mathbf{Q}_{p013}}{\|\mathbf{Q}_{013}\| \cdot \|\mathbf{Q}_{p013}\|} \quad (29)$$

$$\pm \cos \chi_0 = \frac{\mathbf{Q}_{012} \cdot \mathbf{Q}_{023}}{\|\mathbf{Q}_{012}\| \cdot \|\mathbf{Q}_{023}\|} \quad (30)$$

$$\pm \cos \chi = \cos \zeta \cdot \sqrt{1 - (V_{12}/V_{23})^2 (1 - \cos^2 \zeta)} - (V_{12}/V_{23})(1 - \cos^2 \zeta) \quad (31)$$

$$\pm \cos \chi_{p0} = \frac{\mathbf{Q}_{p012} \cdot \mathbf{Q}_{p023}}{\|\mathbf{Q}_{p012}\| \cdot \|\mathbf{Q}_{p023}\|} \quad (32)$$

$$\sin \chi_p = \frac{2V_{13} \cos \zeta_z \sin \zeta_p}{\sqrt{(V_{23})^2 - (2V_{13} \sin \zeta_z)^2}} \quad (33)$$

$$\pm \cos \chi_{z0} = \frac{\mathbf{Q}_{023} \cdot \mathbf{Q}_{p023}}{\|\mathbf{Q}_{023}\| \cdot \|\mathbf{Q}_{p023}\|} \quad (34)$$

$$\sin \chi_z = \frac{2V_{13} \sin \zeta_z}{V_{23}} \quad (35)$$

χ_{z0} and ζ_{z0} are defined positive if the z-components of \mathbf{Q}_{023} and \mathbf{Q}_{013} are positive and vice versa. χ_z has the same sign as the user-defined angle ζ_z . Sign conventions for remaining angles are summarized in Table 2, fitting Equations (36–39) and Figure 5–12 in section 3.2.

Angles	Antenna looking...	Triangle opening...	Sign
$\chi_0, \chi, \chi_{p0}, \chi_p$	left.	left.	+
$\zeta_0, \zeta, \zeta_{p0}, \zeta_p$	left.	left.	+
$\chi_0, \chi, \chi_{p0}, \chi_p$	left.	right.	–
$\zeta_0, \zeta, \zeta_{p0}, \zeta_p$	left.	right.	–
$\chi_0, \chi, \chi_{p0}, \chi_p$	right.	right.	+
$\zeta_0, \zeta, \zeta_{p0}, \zeta_p$	right.	right.	+
$\chi_0, \chi, \chi_{p0}, \chi_p$	right.	left.	–
$\zeta_0, \zeta, \zeta_{p0}, \zeta_p$	right.	left.	–

Table 2 resumes signs of 3-dimensional- and horizontal angles. Note that when varying the geometry, the user-defined angle ζ_p sets the opening direction of the triangle. Equations (40–43) expect all signs inverted.

3.2 The Merging transform

The M-transform converts polar coordinates of full aperture images to polar coordinates of sub-images. This conforms to geometry variations such as: translations and rotations in the xy-plane [9, 10, 12].

There are eight scenarios to consider, i.e. the permutations given by two sub-apertures, two antenna directions (left/right) and two opening directions (left/right) of the sub-aperture triangle. In principle, eight permutations result in 16 equations, eight calculating range and eight calculating sub-lobe angle. However, due to symmetries, half of the equations are redundant. For a practical realization, sign conventions (see section 3.1 and 3.4) permit another factor two reduction. Upcoming pages illustrate the scenarios. The equations are summarized below and on the next page, corresponding figures are pointed out, making the mentioned symmetries rather obvious.

$$R_{M12} = (R_{d13}^2 + (V_{p23}T/2)^2 - R_{d13}V_{p23}T \cos(\pi - \Phi_{d13} + \chi_p - \zeta_p))^{1/2} \quad (36)$$

$$\Phi_{M12} = \arccos((R_{d13}^2 - R_{M12}^2 - (V_{p23}T/2)^2) / (-R_{M12}V_{p23}T)) + \chi_p \quad (37)$$

See Figure 5 and 9. The cosine theorem confirms the equations.

$$R_{M23} = (R_{d13}^2 + (V_{p12}T/2)^2 - R_{d13}V_{p12}T \cos(\Phi_{d13} + \zeta_p))^{1/2} \quad (38)$$

$$\Phi_{M23} = \pi - \chi_p - \arccos((R_{d13}^2 - R_{M23}^2 - (V_{p12}T/2)^2) / (-R_{M23}V_{p12}T)) \quad (39)$$

See Figure 6 and 10. The cosine theorem confirms the equations.

$$R_{M12} = (R_{d13}^2 + (V_{p23}T/2)^2 - R_{d13}V_{p23}T \cos(\pi - \Phi_{d13} - \chi_p + \zeta_p))^{1/2} \quad (40)$$

$$\Phi_{M12} = \arccos((R_{d13}^2 - R_{M12}^2 - (V_{p23}T/2)^2) / (-R_{M12}V_{p23}T)) - \chi_p \quad (41)$$

See Figure 7 and 11. The cosine theorem confirms the equations.

$$R_{M23} = (R_{d13}^2 + (V_{p12}T/2)^2 - R_{d13}V_{p12}T \cos(\Phi_{d13} - \zeta_p))^{1/2} \quad (42)$$

$$\Phi_{M23} = \pi + \chi_p - \arccos((R_{d13}^2 - R_{M23}^2 - (V_{p12}T/2)^2) / (-R_{M23}V_{p12}T)) \quad (43)$$

See Figure 8 and 12. The cosine theorem confirms the equations.

If the autofocus algorithm is applied at the beginning of the factorization, crossing situations may occur. For example: a left looking SAR system turning into a right looking SAR system and the other way around. For long sub-apertures (or integration times) and minor departures from the ideal track (as in this case), these issues are of no concern.

In Revision B, Equations (36–43) are somewhat modified, α_{12} and α_{23} introduced in section 3.4 replace ζ_p and $(\chi_p - \zeta_p)$ respectively.

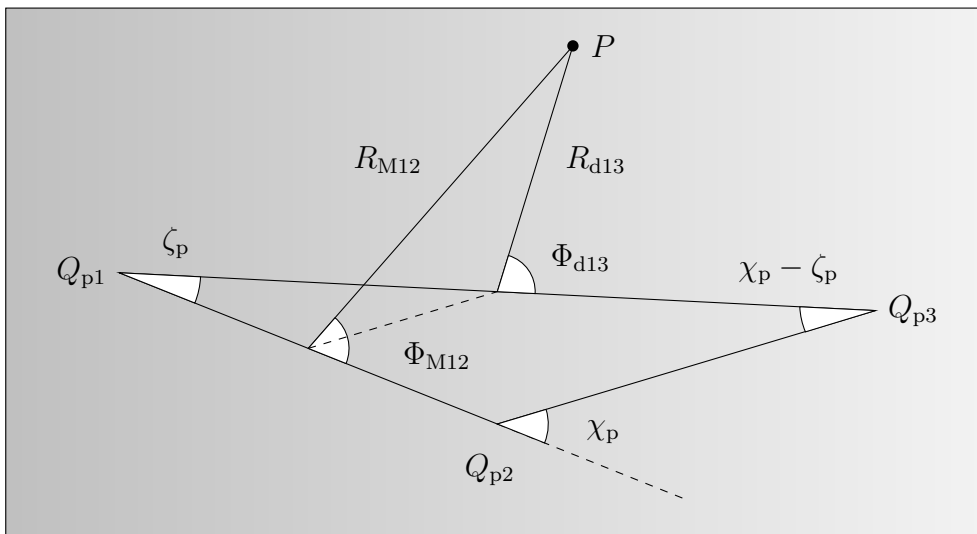


Figure 5 shows the merging geometry, expressing the polar coordinates of the full aperture Q_{p13} in coordinates of sub-aperture Q_{p12} . Left looking antenna, left opening triangle. P is some point of interest on the ground.

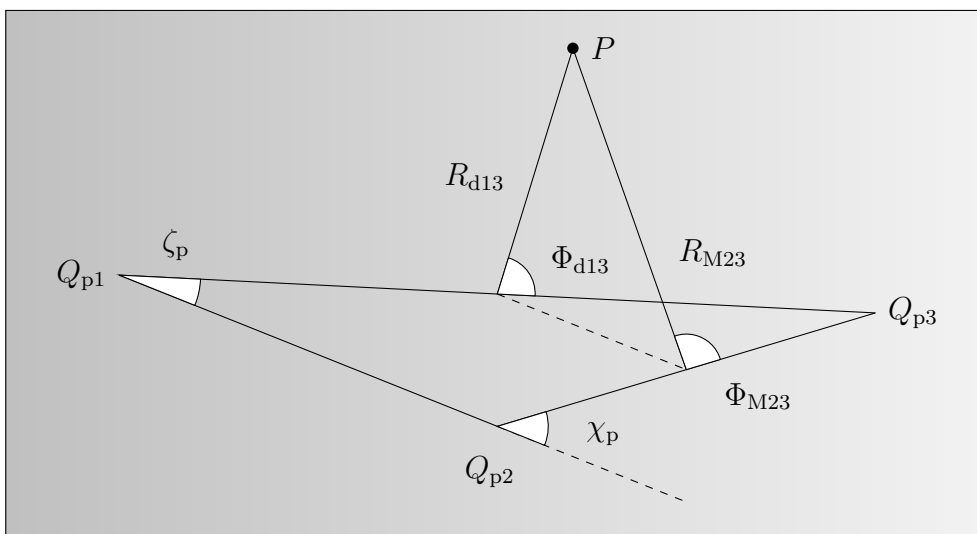


Figure 6 shows the merging geometry, expressing the polar coordinates of the full aperture Q_{p13} in coordinates of sub-aperture Q_{p23} . Left looking antenna, left opening triangle. P is some point of interest on the ground.

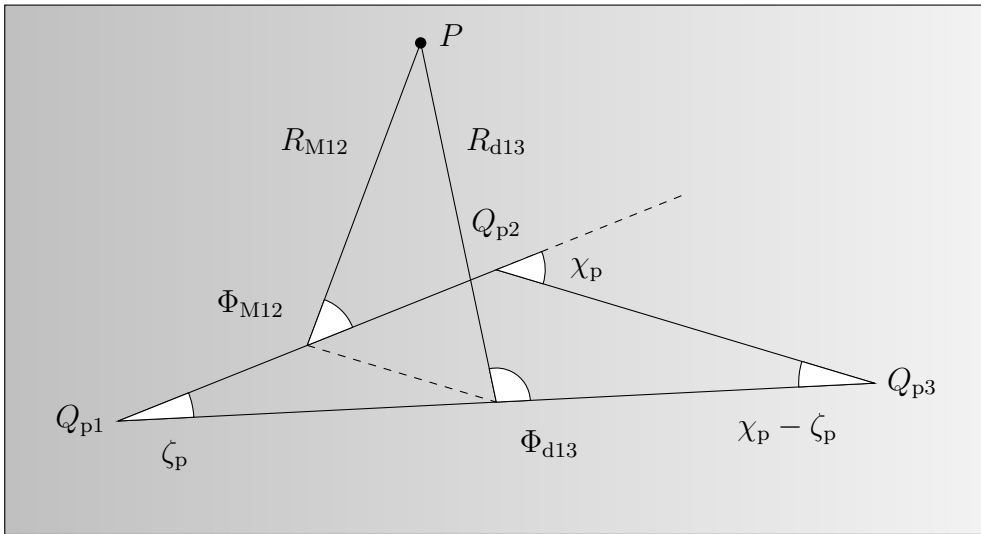


Figure 7 shows the merging geometry, expressing the polar coordinates of the full aperture Q_{p13} in coordinates of sub-aperture Q_{p12} . Left looking antenna, right opening triangle. P is some point of interest on the ground.

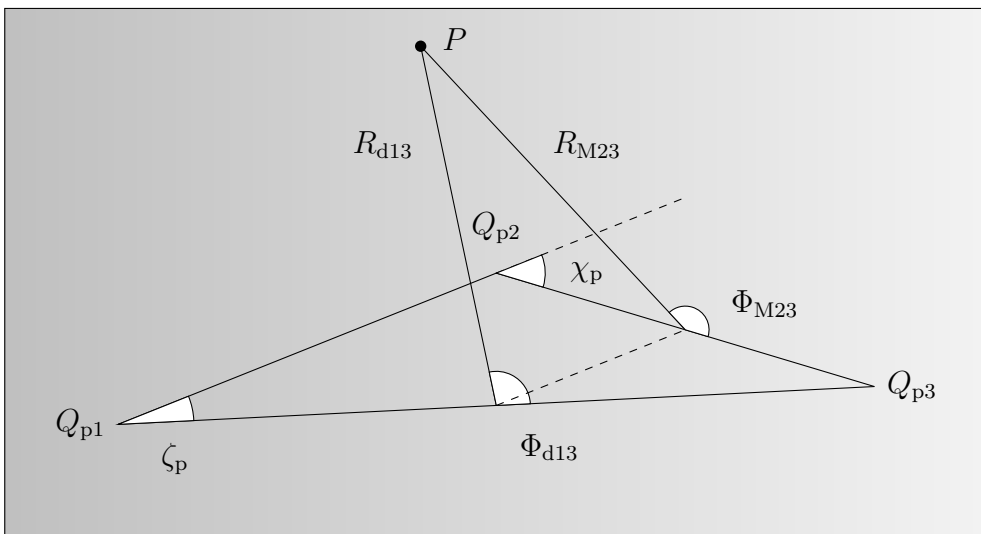


Figure 8 shows the merging geometry, expressing the polar coordinates of the full aperture Q_{p13} in coordinates of sub-aperture Q_{p23} . Left looking antenna, right opening triangle. P is some point of interest on the ground.

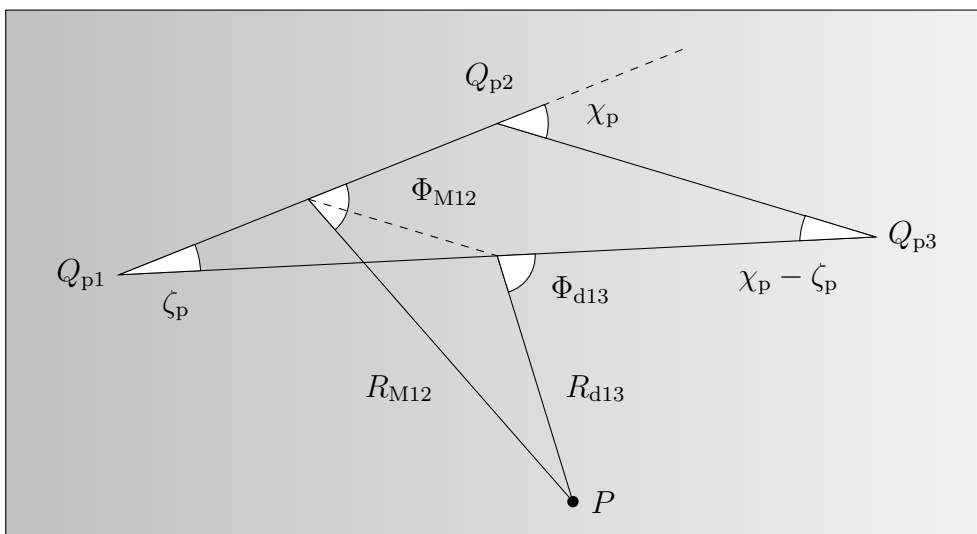


Figure 9 shows the merging geometry, expressing the polar coordinates of the full aperture Q_{p13} in coordinates of sub-aperture Q_{p12} . Right looking antenna, right opening triangle. P is some point of interest on the ground.

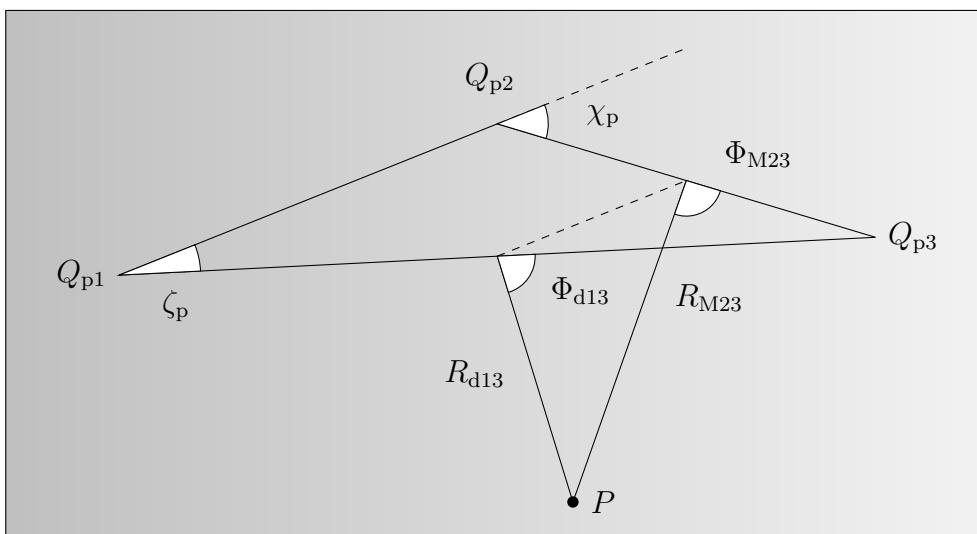


Figure 10 shows the merging geometry, expressing the polar coordinates of the full aperture Q_{p13} in coordinates of sub-aperture Q_{p23} . Right looking antenna, right opening triangle. P is some point of interest on the ground.

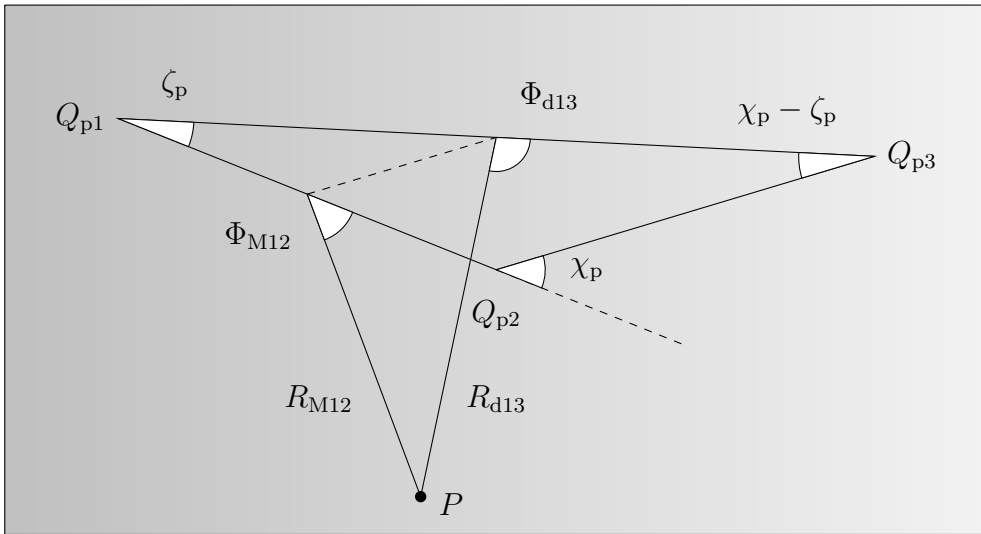


Figure 11 shows the merging geometry, expressing the polar coordinates of the full aperture Q_{p13} in coordinates of sub-aperture Q_{p12} . Right looking antenna, left opening triangle. P is some point of interest on the ground.

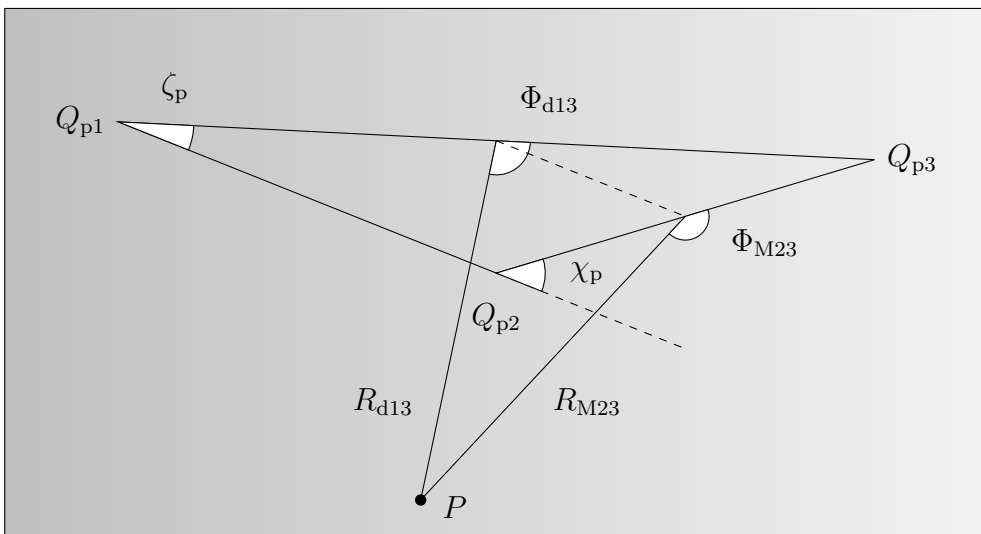


Figure 12 shows the merging geometry, expressing the polar coordinates of the full aperture Q_{p13} in coordinates of sub-aperture Q_{p23} . Right looking antenna, left opening triangle. P is some point of interest on the ground.

3.3 The Range History Preserving transform

The RHP-transform distorts M-transformed coordinates. This conforms to geometry variations such as: vertical tilts, altitude- and speed alterations [9, 10, 12]. As opposed to the M-transform, the RHP-transform works with individual sub-apertures. Consider \mathbf{Q}_0 , defined between $-T/2 < t < T/2$.

The slant range to the point \mathbf{P} as a function of time is given by Equation (44).

$$\begin{aligned} \|\mathbf{Q}_0(t)\mathbf{P}\| &= ((R_M \sin \Phi_M)^2 + (R_M \cos \Phi_M - V_{p0}t)^2 \\ &\quad + (H_0 + V_{z0}t)^2)^{1/2} \end{aligned} \quad (44)$$

R_M is the M-transformed ground range to \mathbf{P} at $t = 0$.

Φ_M is the M-transformed ground sub-lobe angle at $t = 0$.

V_{p0} is the horizontal speed, while V_{z0} is the vertical velocity.

H_0 is the altitude (the midpoint altitude) at $t = 0$.

Now consider \mathbf{Q} , defined for the same t as before, but with altered horizontal speed (V_p), vertical velocity (V_z) and altitude (H).

The slant range to the point \mathbf{P} as a function of time is given by Equation (45).

$$\begin{aligned} \|\mathbf{Q}(t)\mathbf{P}\| &= ((R_M \sin \Phi_M)^2 + (R_M \cos \Phi_M - V_p t)^2 \\ &\quad + (H + V_z t)^2)^{1/2} \end{aligned} \quad (45)$$

The RHP-transform replace R_M and Φ_M in Equation (44) with primed parameters R'_M and Φ'_M . The objective is to find an equality or at least an approximate equality between the range histories of $\|\mathbf{Q}(t)\mathbf{P}\|$ and $\|\mathbf{Q}'_0(t)\mathbf{P}\|$.

This can be accomplished by first expanding the primed version of Equation (44) and Equation (45) respectively. Setting the resulting polynomial coefficients (t) to agree, then gives expressions for R'_M and Φ'_M .

$$R'_M + H_0^2 = R_M^2 + H^2 \quad (46)$$

$$R'_M V_{p0} \cos \Phi'_M - H_0 V_{z0} = R_M V_p \cos \Phi_M - H V_z \quad (47)$$

$$\begin{cases} V_{p0}^2 + V_{z0}^2 = V_p^2 + V_z^2 & \text{if } V_p = \sqrt{V_{p0}^2 + V_{z0}^2 - V_z^2} \\ V_{p0}^2 + V_{z0}^2 \neq V_p^2 + V_z^2 & \text{if } V_p \neq \sqrt{V_{p0}^2 + V_{z0}^2 - V_z^2} \end{cases} \quad (48)$$

$$R'_M = \sqrt{R_M^2 + H^2 - H_0^2} \quad (49)$$

$$\Phi'_M = \arccos\left(\frac{(R_M V_p \cos \Phi_M - H V_z + H_0 V_{z0})}{(R'_M V_{p0})}\right) \quad (50)$$

The equality in Equation (46) is satisfied by the relationship in Equation (49).

The equality in Equation (47) is satisfied by the relationship in Equation (50).

The equality in Equation (48) is not always satisfied, if not, defocusing effects will be experienced. These may however be negligible for a minor inequality, thus speed alterations¹⁸ are allowed when varying the geometry. For a horizontal sub-aperture, an alteration as large as the linear cross-range resolution divided by the integration time is permitted [9, 10]. This implies that the ability to compensate for measurement errors concerning speed, is much higher at the beginning of the factorization than at the end¹⁹.

This report assumes that the equality in Equation (48) is satisfied.

¹⁸Overall speed alterations, vertical velocity included.

¹⁹At the final factorization step, measurement errors on the order of cm/s can be compensated for.

3.4 Revision B

In Revision B [10], \mathbf{Q}_{13} (with \mathbf{Q}_{013} as a special case) is presumed to be parallel to the xy -plane at all times. Hence, an interpolation routine must modify focused sub-image pairs in agreement with necessary geometry changes. If the algorithm is applied at the final factorization step, the routine²⁰ may be implemented prior to the ground projection (in the slant plane).

The assumed geometry is established in the figure below, while the upcoming table enumerates all significant parameters.

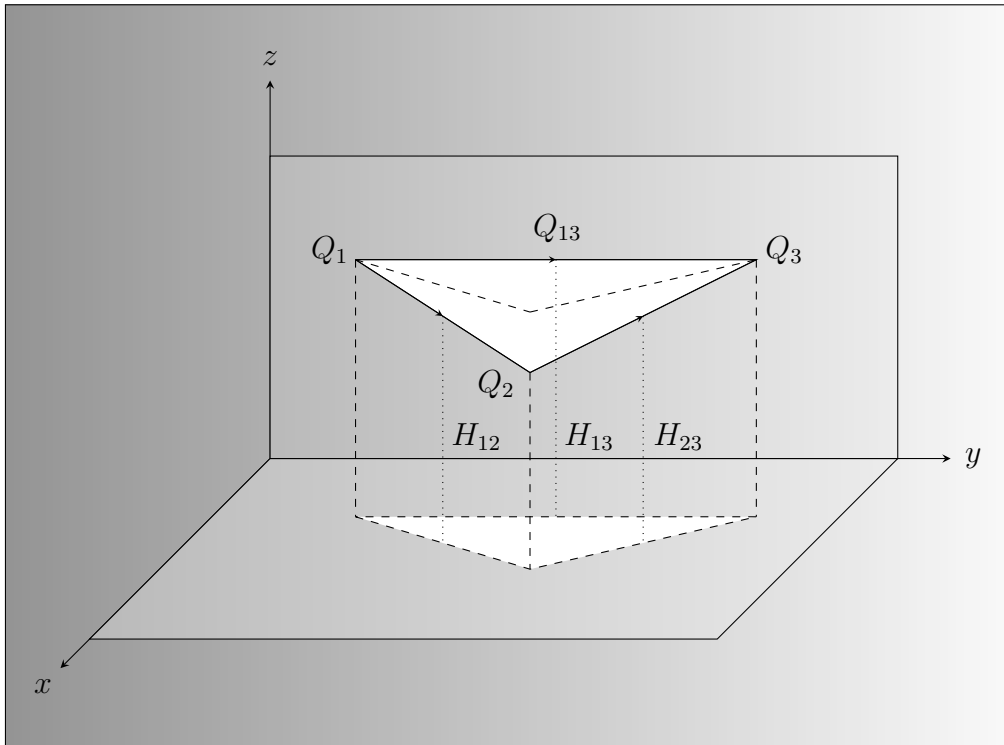


Figure 13 shows the Rev. B geometry, all vectors are not denoted, but understood from Figure 3. Notice that \mathbf{Q}_{13} is parallel to the horizontal plane, also note that altitudes are marked out for clarification.

²⁰Since this interpolation routine is very similar to the one described in section 3.5, it will not be discussed further in this report.

Table 3 resumes the notations of Rev. B parameters, short descriptions and some comments are also tabulated. Table 3 continues on the next page.

Notation	Description	Comment
Q_{01}, Q_{02}, Q_{03}	Start-, cut-off- and end point of flight track (x,y,z) (m).	Constant quantities, given, navigation parameters.
$Q_{p01}, Q_{p02}, Q_{p03}$	Projected points (x,y) (m).	Constant quantities, given.
$Q_{012}, Q_{023}, Q_{013}$	Initial direction vectors (x,y,z) (m).	Constant quantities, derived, section 3.1.
$Q_{p012}, Q_{p023}, Q_{p013}$	Projected vectors (x,y) (m).	Constant quantities, derived, section 3.1.
Q_{12}, Q_{23}, Q_{13}	Updated direction vectors (x,y,z) (m).	Varying quantities, not derived.
$Q_{p12}, Q_{p23}, Q_{p13}$	Projected vectors (x,y) (m).	Varying quantities, not derived.
$H_{012}, H_{023}, H_{013}$	Initial altitudes (midpoints) (m).	Constant quantities, derived.
H_{12}, H_{23}, H_{13}	Updated altitudes (midpoints) (m).	Varying quantities, derived.
PRF	Pulse Repetition Frequency (Hz).	Constant quantity, given.
N	Number of pulses for one sub-aperture.	Constant quantity, given.
T	Travel time for one sub-aperture (s).	Constant quantity, derived, section 3.1.
$V_{012}, V_{023}, V_{013}$	Initial speeds (m/s).	Constant quantities, derived, section 3.1.
V_{12}, V_{23}	Updated speeds (m/s).	Variation quantities, user-defined values.
V_{13}	Updated speed (m/s).	Varying quantity, derived, section 3.1.
V_{p012}, V_{p023}	Initial horizontal speeds (m/s).	Constant quantities, derived, section 3.1.
V_{p12}, V_{p23}	Updated horizontal speeds (m/s).	Varying quantities, derived, section 3.1.
V_{z012}, V_{z023}	Initial vertical velocities (signed) (m/s).	Constant quantities, derived.

Notation	Description	Comment
V_{z12}, V_{z23}	Updated vertical velocities (signed) (m/s).	Varying quantities, derived.
ψ_0	Angle between \mathbf{Q}_{0123} -plane and xy-plane (rad).	Constant quantity, derived.
ψ	Angle between \mathbf{Q}_{123} -plane and xy-plane (rad).	Variation quantity, user-defined values.
χ_0	Angle between \mathbf{Q}_{012} and \mathbf{Q}_{023} (rad).	Constant quantity, derived, section 3.1.
χ	Angle between \mathbf{Q}_{12} and \mathbf{Q}_{23} (rad).	Variation quantity, user-defined values.
α_{012}	Angle between \mathbf{Q}_{p013} and \mathbf{Q}_{p012} (rad).	Constant quantity, derived.
α_{023}	Angle between \mathbf{Q}_{p013} and \mathbf{Q}_{p023} (rad).	Constant quantity, derived.
α_{12}	Angle between \mathbf{Q}_{p13} and \mathbf{Q}_{p12} (rad).	Varying quantity, derived.
α_{23}	Angle between \mathbf{Q}_{p13} and \mathbf{Q}_{p23} (rad).	Varying quantity, derived.
β_{012}	Angle between \mathbf{Q}_{012} and \mathbf{Q}_{p012} (rad).	Constant quantity, derived.
β_{023}	Angle between \mathbf{Q}_{023} and \mathbf{Q}_{p023} (rad).	Constant quantity, derived.
β_{12}	Angle between \mathbf{Q}_{12} and \mathbf{Q}_{p12} (rad).	Varying quantity, derived.
β_{23}	Angle between \mathbf{Q}_{23} and \mathbf{Q}_{p23} (rad).	Varying quantity, derived.
$R_{d12}, R_{d23}, R_{d13}$	Ground ranges (discrete values) (m).	Constant quantities, see section 3.5.
$\Phi_{d12}, \Phi_{d23}, \Phi_{d13}$	Ground sub-lobe angles (discrete values) (rad).	Constant quantities, see section 3.5.
R_{M12}, R_{M23}	M-transformed ground ranges (m).	Varying quantities, derived, section 3.2.
Φ_{M12}, Φ_{M23}	M-transformed ground sub-lobe angles (rad).	Varying quantities, derived, section 3.2.
R'_{M12}, R'_{M23}	M- and RHP-transformed ground ranges (m).	Varying quantities, derived, section 3.3.
Φ'_{M12}, Φ'_{M23}	M- and RHP-transformed ground sub-lobe angles (rad).	Varying quantities, derived, section 3.3.

In Table 3, angles denoted by the Greek letter Φ are defined between 0 and π , all other angles are defined between $-\pi/2$ and $\pi/2$. A subscript zero indicates an initial state, while a p stands for projected. Quantities will now be derived by means of given system-/track parameters and user-defined variables.

$$H_{013} = (Q_{01_z} + Q_{03_z})/2 \quad (51)$$

$$H_{13} = H_{013} \quad (52)$$

$$H_{012} = \frac{V_{012}T}{2} \cdot \sin \beta_{012} + H_{013} \quad (53)$$

$$H_{12} = \frac{V_{12}T}{2} \cdot \sin \beta_{12} + H_{13} \quad (54)$$

$$H_{023} = \frac{V_{023}T}{2} \cdot \sin \beta_{023} + H_{013} \quad (55)$$

$$H_{23} = \frac{V_{23}T}{2} \cdot \sin \beta_{23} + H_{13} \quad (56)$$

$$V_{z012} = V_{012} \cdot \sin \beta_{012} \quad (57)$$

$$V_{z023} = -V_{023} \cdot \sin \beta_{023} \quad (58)$$

$$V_{z12} = V_{12} \cdot \sin \beta_{12} \quad (59)$$

$$V_{z23} = -V_{23} \cdot \sin \beta_{23} \quad (60)$$

$$\pm \cos \psi_0 = \left\| \left(\frac{\mathbf{Q}_{012} \times \mathbf{Q}_{013}}{\|\mathbf{Q}_{012} \times \mathbf{Q}_{013}\|} \right) \cdot \hat{\mathbf{k}} \right\| \quad (61)$$

$$\pm \cos \alpha_{012} = \frac{\mathbf{Q}_{p013} \cdot \mathbf{Q}_{p012}}{\|\mathbf{Q}_{p013}\| \cdot \|\mathbf{Q}_{p012}\|} \quad (62)$$

$$\sin \alpha_{12} = \frac{V_{23} \sin \chi \cos \psi}{\sqrt{V_{12}^2 + V_{23}^2 + 2V_{12}V_{23} \cos \chi - V_{23}^2 (\sin \chi \sin \psi)^2}} \quad (63)$$

$$\pm \cos \alpha_{023} = \frac{\mathbf{Q}_{p013} \cdot \mathbf{Q}_{p023}}{\|\mathbf{Q}_{p013}\| \cdot \|\mathbf{Q}_{p023}\|} \quad (64)$$

$$\sin \alpha_{23} = \frac{V_{12} \sin \chi \cos \psi}{\sqrt{V_{12}^2 + V_{23}^2 + 2V_{12}V_{23} \cos \chi - V_{12}^2 (\sin \chi \sin \psi)^2}} \quad (65)$$

$$\pm \cos \beta_{012} = \frac{\mathbf{Q}_{012} \cdot \mathbf{Q}_{p012}}{\|\mathbf{Q}_{012}\| \cdot \|\mathbf{Q}_{p012}\|} \quad (66)$$

$$\tan \beta_{12} = \frac{V_{23} \sin |\chi| \sin \psi}{\sqrt{V_{12}^2 + V_{23}^2 + 2V_{12}V_{23} \cos \chi - V_{23}^2 (\sin \chi \sin \psi)^2}} \quad (67)$$

$$\pm \cos \beta_{023} = \frac{\mathbf{Q}_{023} \cdot \mathbf{Q}_{p023}}{\|\mathbf{Q}_{023}\| \cdot \|\mathbf{Q}_{p023}\|} \quad (68)$$

$$\tan \beta_{23} = \frac{V_{12} \sin |\chi| \sin \psi}{\sqrt{V_{12}^2 + V_{23}^2 + 2V_{12}V_{23} \cos \chi - V_{12}^2 (\sin \chi \sin \psi)^2}} \quad (69)$$

β_{012} , β_{023} and ψ_0 are defined positive if the z-components of $\mathbf{Q}_{012}/\mathbf{Q}_{023}$ are positive/negative and vice versa. β_{12} and β_{23} have the same sign as the user-defined angle ψ . Sign conventions for remaining angles are summarized in Table 4, fitting Equations (36–39) and Figure 5–12 in section 3.2.

Angles	Antenna looking...	Triangle opening...	Sign
χ_0, χ	left.	left.	+
$\alpha_{012}, \alpha_{12}, \alpha_{023}, \alpha_{23}$	left.	left.	+
χ_0, χ	left.	right.	–
$\alpha_{012}, \alpha_{12}, \alpha_{023}, \alpha_{23}$	left.	right.	–
χ_0, χ	right.	right.	+
$\alpha_{012}, \alpha_{12}, \alpha_{023}, \alpha_{23}$	right.	right.	+
χ_0, χ	right.	left.	–
$\alpha_{012}, \alpha_{12}, \alpha_{023}, \alpha_{23}$	right.	left.	–

Table 4 resumes signs of 3-dimensional- and horizontal angles. Note that when varying the geometry, the user-defined angle χ sets the opening direction of the triangle. Equations (40–43) expect all signs inverted.

3.5 Preprocessing

The moment the autofocus algorithm is activated, conventional slant images must be projected to the ground plane. This is a step by step procedure, which now will be described briefly.

First, Cartesian coordinates corresponding to lobe-ground intersections are located. Details concerning the slant-to-ground conversion can be found in Appendix II. Next, ranges and sub-lobe angles to the retrieved coordinates are computed. The centre point of the projected sub-aperture represents the origin, while the projected direction vector is the angular reference.

At this time, the polar grid is not equidistant. Therefore it is linearized before being converted back to Cartesian coordinates. Next, ranges and sub-lobe angles to the altered coordinates are computed. The centre point of the (3-dimensional) sub-aperture represents the origin, while the (3-dimensional) direction vector is the angular reference. Interpolation in the slant plane finally gives the projected image. Ground ranges and ground sub-lobe angles are defined when the grid is linearized. Before moving on, it should be mentioned that the angular dimension usually is sampled in cosine of sub-lobe angles. In fact, this is the case for the data sets in this report. Regardless, basic principles apply, thus the terminology adopted this far prevails.

Upcoming images have been processed with a sinc interpolator (64 coefficients), weighted with a Kaiser window (two 1-dimensional runs). The β -value²¹ of the window was set to 2.5, broadening the Impulse Response Width (IRW) or 3-dB width by $\sim 20\%$, while suppressing the sidelobes by ~ 20 dB.

As CARABAS II data resides on the centre frequency, the interpolator should be shifted by means of an exponential phase ramp. This has not been put into practice, since the data is deemed sufficiently oversampled²².

More information regarding sinc interpolators and smoothing windows can be found in most fundamental signal processing books, for example [19]. Another recommended reference is [4], limiting the math to a minimum.

²¹Not to be confused with any of the β angles in Revision B.

²²The slant plane data is upsampled by a factor four in the range dimension and by a factor two in the angular dimension.

3.6 Image formation & Object functions

Every single geometry hypothesis generates two sub-images (G_{p12}/G_{p23}), a coherent addition of these produces the final image (G_{p13}), see Equation (70). The focus measure obtained from the assigned object function then settles whether this full aperture image is the true one or not. The object functions considered are as mentioned in the introduction: correlation [9, 10, 12], entropy [27] and maximum intensity [18], see Equations (71–73).

$$\begin{aligned}
 G_{p13}(R_{d13}, \Phi_{d13}) &= G_{p12}(R'_{M12}, \Phi'_{M12}) & (70) \\
 &\cdot e^{\frac{j4\pi(\sqrt{R'^2_{M12}+H^2_{012}}-\sqrt{R^2_{d12}+H^2_{012}})}{\lambda}} \\
 &+ G_{p23}(R'_{M23}, \Phi'_{M23}) \\
 &\cdot e^{\frac{j4\pi(\sqrt{R'^2_{M23}+H^2_{023}}-\sqrt{R^2_{d23}+H^2_{023}})}{\lambda}}
 \end{aligned}$$

Factorized radar echoes, $G_{p12}(R_{d12}, \Phi_{d12})$ and $G_{p23}(R_{d23}, \Phi_{d23})$, are assumed to be range compressed, with the carrier preserved intact. Note that R_{d12} and R_{d23} represent discrete ground range bins, while Φ_{d12} and Φ_{d23} represent discrete ground sub-lobe angles. This implies that interpolation of factorized echoes is a necessity to find $G_{p12}(R'_{M12}, \Phi'_{M12})$ and $G_{p23}(R'_{M23}, \Phi'_{M23})$. The exponential functions are bandpass phase factors (nearest neighbour phase factors), with carrier wavelength λ .

$$C = \sum \sum (|G_{p12}|^2 \cdot |G_{p23}|^2) \quad (71)$$

$$E = - \sum \sum \left(\left(\frac{|G_{p13}|^2}{\sum \sum |G_{p13}|^2} \right) \ln \left(\frac{|G_{p13}|^2}{\sum \sum |G_{p13}|^2} \right) \right) \quad (72)$$

$$I_{\max} = \max \left(|G_{p13}|^2 \right) \quad (73)$$

3.7 Scenes

The algorithm will be evaluated through tests on two different data sets. Upcoming pages will show two deterministically focused full aperture images (focused by means of available navigation data) for each set or scene. One for Revision A [9] and one for Revision B [10]. These images are very similar, but shown to emphasize that Rev. A results are compared to the Rev. A references and that Rev. B results are compared to the Rev. B references.

The first scene is Vidsel, a very sparse rural setting, distinctive features include among other things a trihedral reflector and a power line structure. Corresponding images can be studied in Figure 14 and 15.

The second scene is Linköping, a complex urban setting, displaying a plethora of features. Corresponding images can be studied in Figure 16 and 17.

It should be pointed out, that some of the targets (buildings) in these images appear to be split into two parts, whether this is due to a scattering mechanism (double bounce) or a processing bug is not clear for the time being.

3.8 Evaluation procedure

Revision A [9] and Revision B [10] have four independent parameters (two in common), visualizing a focus measure in four dimensions is not viable. Therefore, two of the parameters (V_{12}/V_{23}) will be held constant (set to initial values/subscript zero values) when testing the algorithm.

For Rev. A the following geometry variation will be executed:

- ζ_p vs. ζ_z

For Rev. B the following geometry variation will be executed:

- χ vs. ψ

For the first scene (Vidsel), maximum intensity values of the trihedral reflector, before and after autofocusing, will be compared. This together with a visual inspection of image quality (before and after autofocusing) will give some pointers regarding the performance of the algorithm. For the second scene (Linköping), a visual inspection alone will assess the performance.

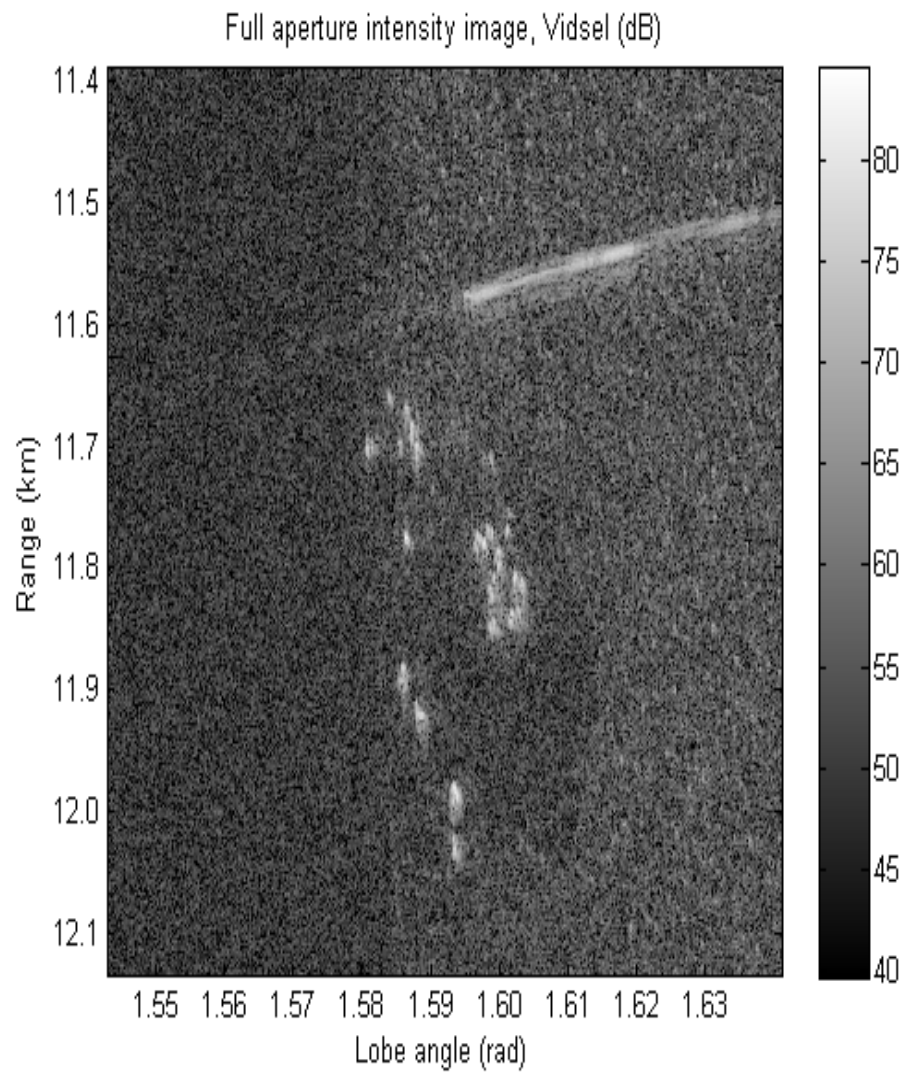


Figure 14 shows the Rev. A reference image of Vidsel, the first scene. The reflector is located at ~ 11780 m and ~ 1.588 rad. The power line is the leaning structure in the top right corner. The size of the image is 1400×700 pixels, with sample spacing ~ 0.5 m and ~ 0.0001 cosine of the sub-lobe angle.

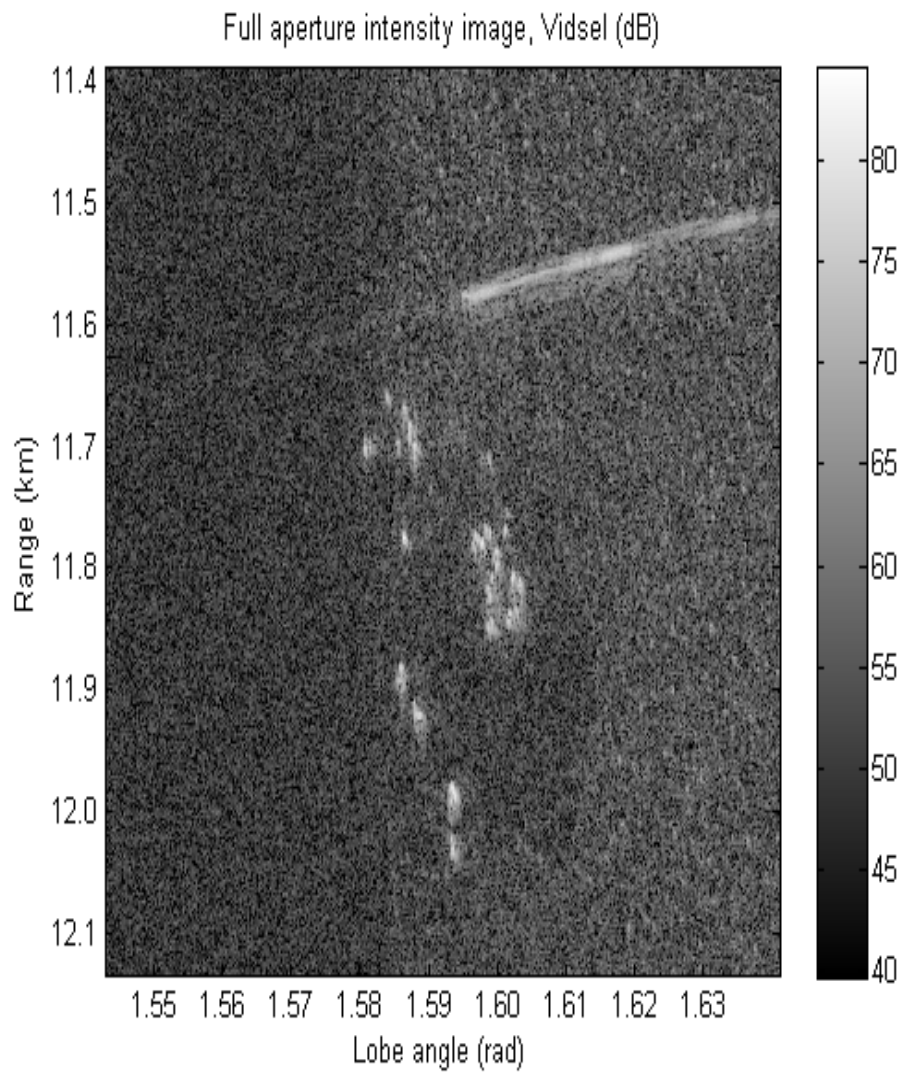


Figure 15 shows the Rev. B reference image of Vidsel, the first scene. The reflector is located at ~ 11780 m and ~ 1.588 rad. The power line is the leaning structure in the top right corner. The size of the image is 1400×700 pixels, with sample spacing ~ 0.5 m and ~ 0.0001 cosine of the sub-lobe angle.

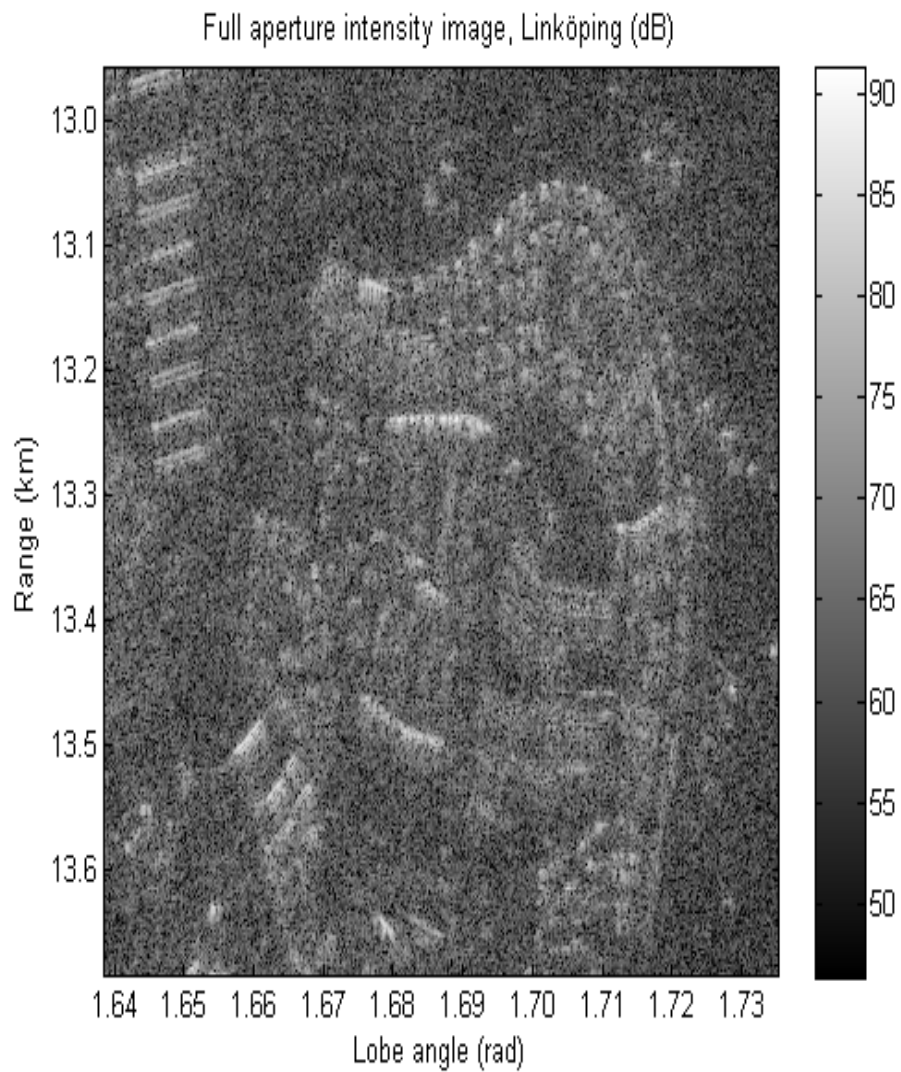


Figure 16 shows the Rev. A reference image of Linköping, the second scene. Split targets are seen in the top left corner. The size of the image is 1400×700 pixels, with sample spacing ~ 0.5 m and ~ 0.0001 cosine of the sub-lobe angle.

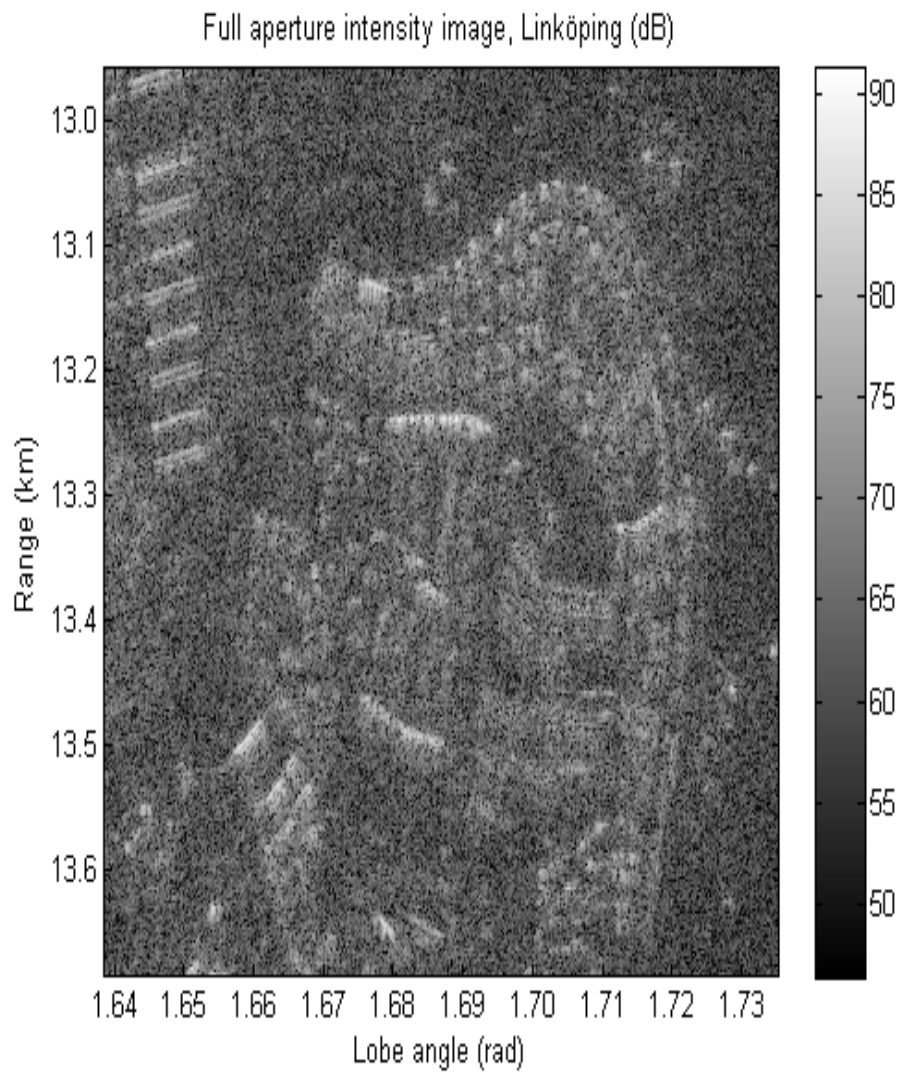


Figure 17 shows the Rev. B reference image of Linköping, the second scene. Split targets are seen in the top left corner. The size of the image is 1400×700 pixels, with sample spacing ~ 0.5 m and ~ 0.0001 cosine of the sub-lobe angle.

4 Results - Revision A

MATLAB results for Revision A [9] will now be presented, along with some minor comments. The complete analysis is found in section 6.

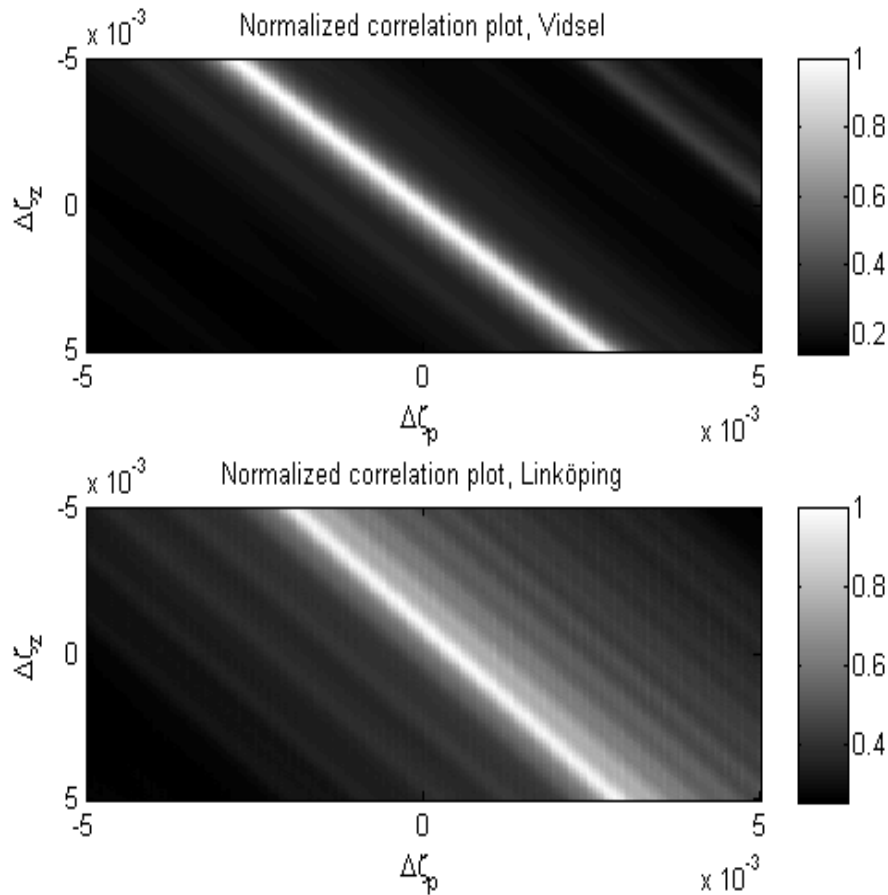


Figure 18 (Top) shows focus measures for Vidsel, while (Bottom) shows focus measures for Linköping. The object function is correlation. Measures corresponding to deterministic solutions are found at the centres of the plots. In other words, the axes display deviations from navigation data in differential variation quantities. The geometry is stepped $50 \mu\text{rad}$ in both dimensions. Before running the algorithm, the first data set was upsampled (additionally) by a factor four (in both range and cosine of sub-lobe angle) to improve the accuracy of the employed nearest neighbour interpolation and consequently the reflector result. This approach does not modify the general appearance of the correlation plot, although peaks and troughs may shift slightly along the ridge.

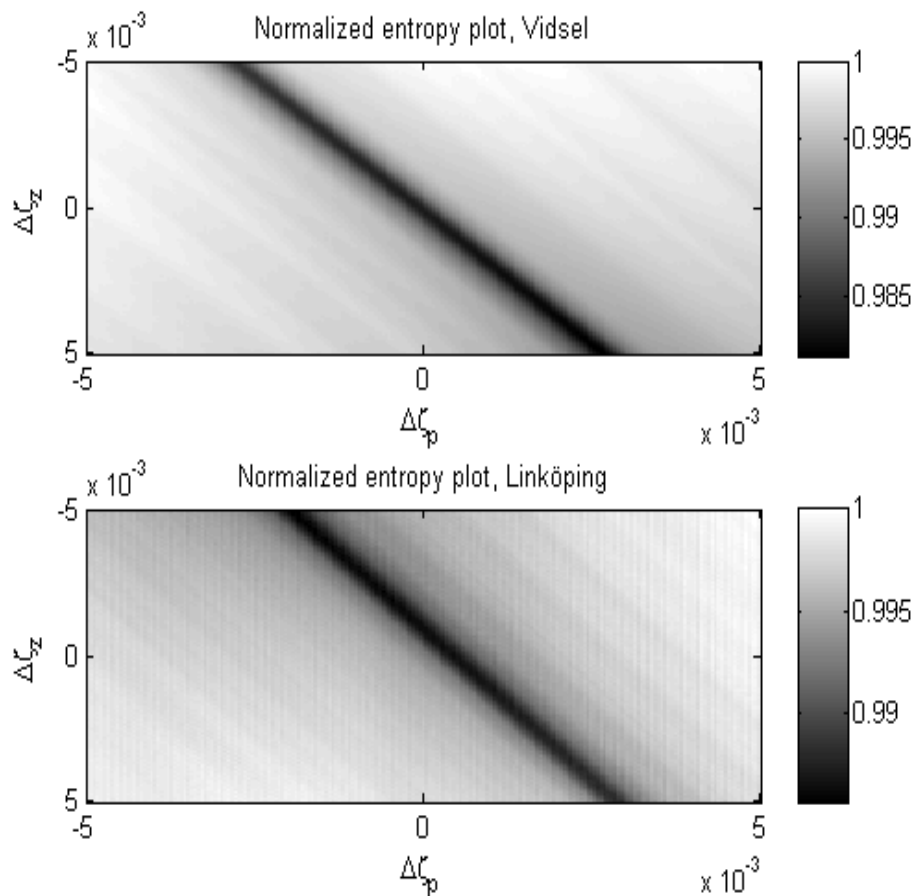


Figure 19 (Top) shows focus measures for Vidsel, while (Bottom) shows focus measures for Linköping. The object function is entropy. Measures corresponding to deterministic solutions are found at the centres of the plots. In other words, the axes display deviations from navigation data in differential variation quantities. The geometry is stepped $50 \mu\text{rad}$ in both dimensions. Before running the algorithm, the first data set was upsampled (additionally) by a factor four (in both range and cosine of sub-lobe angle) to improve the accuracy of the employed nearest neighbour interpolation and consequently the reflector result. This approach does not modify the general appearance of the entropy plot, although peaks and troughs may shift slightly along the ridge.

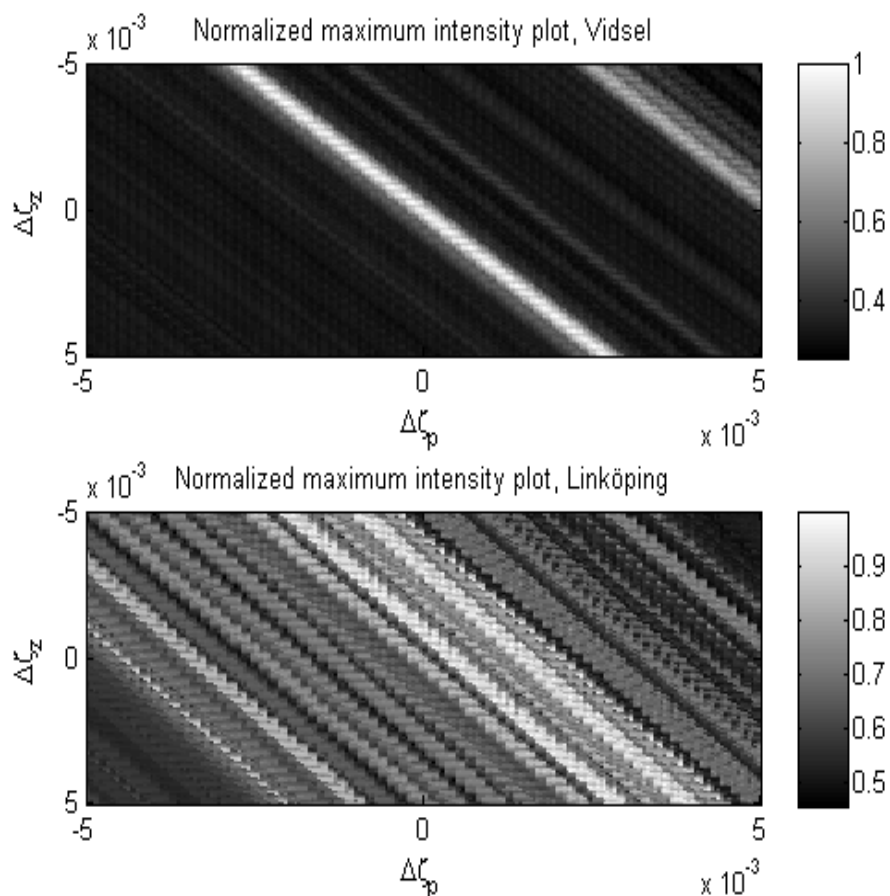


Figure 20 (Top) shows focus measures for Vidsef, while (Bottom) shows focus measures for Linköping. The object function is maximum intensity. Measures corresponding to deterministic solutions are found at the centres of the plots. In other words, the axes display deviations from navigation data in differential variation quantities. The geometry is stepped $50 \mu\text{rad}$ in both dimensions. Before running the algorithm, the first data set was upsampled (additionally) by a factor four (in both range and cosine of sub-lobe angle) to improve the accuracy of the employed nearest neighbour interpolation and consequently the reflector result. This approach does not modify the general appearance of the maximum intensity plot, although peaks and troughs may shift slightly along the ridge.

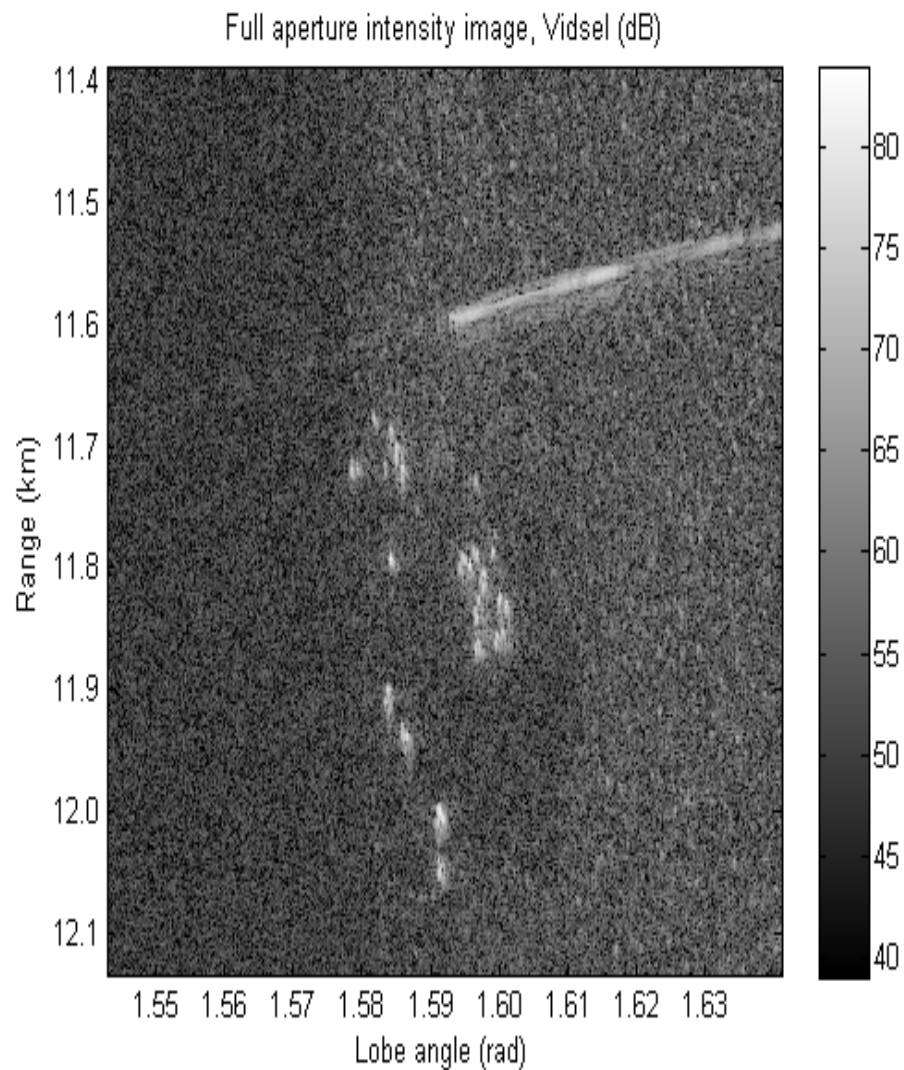


Figure 21 shows an autofocused intensity image of Vidsel. This image corresponds to the highest peak of the correlation plot and can be compared to the deterministically focused image in Figure 14. Note that similar (visually identical) results are acquired for the deepest trough of the entropy plot and the highest peak of the maximum intensity plot. Differential variation values for the peaks and the trough are summarized in Table 5 at the end of this section.

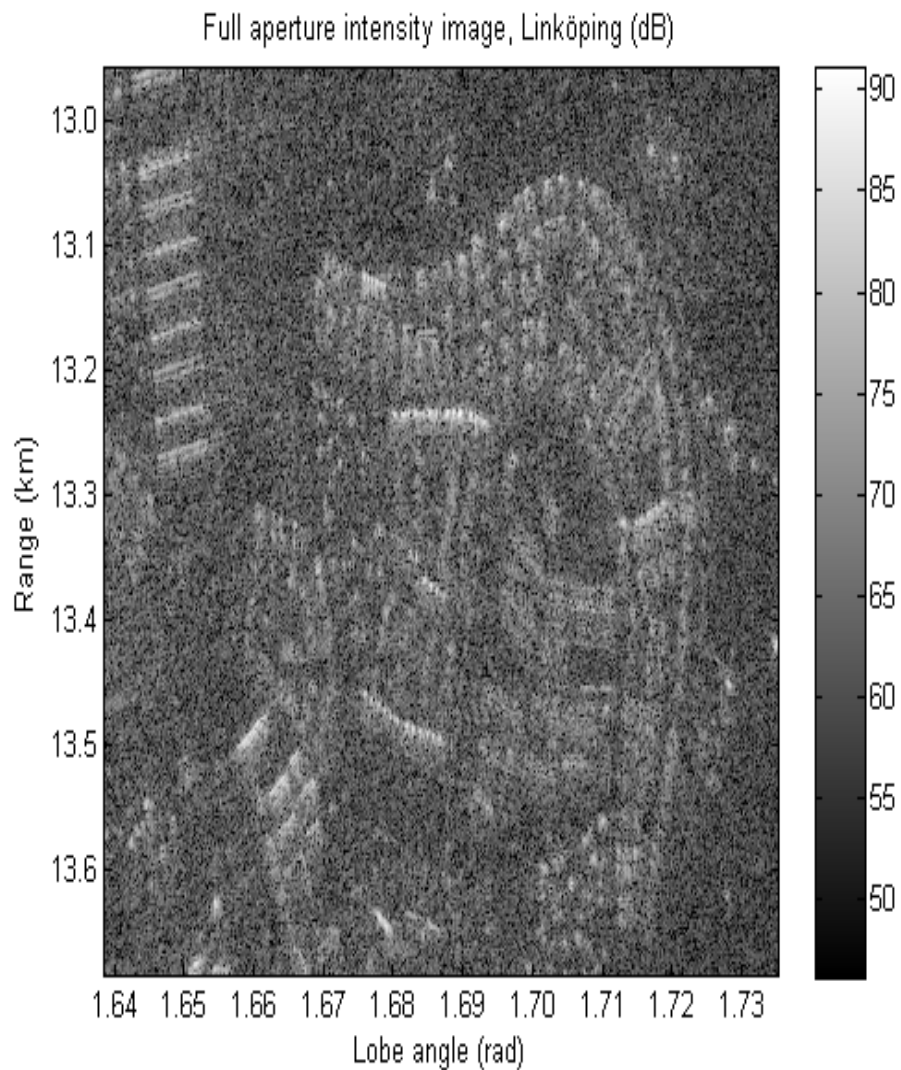


Figure 22 shows an autofocused intensity image of Linköping. This image corresponds to the highest peak of the correlation plot and can be compared to the deterministically focused image in Figure 16. Note that similar (visually identical) results are acquired for the deepest trough of the entropy plot and the highest peak of the maximum intensity plot. Differential variation values for the peaks and the trough are summarized in Table 6 at the end of this section.

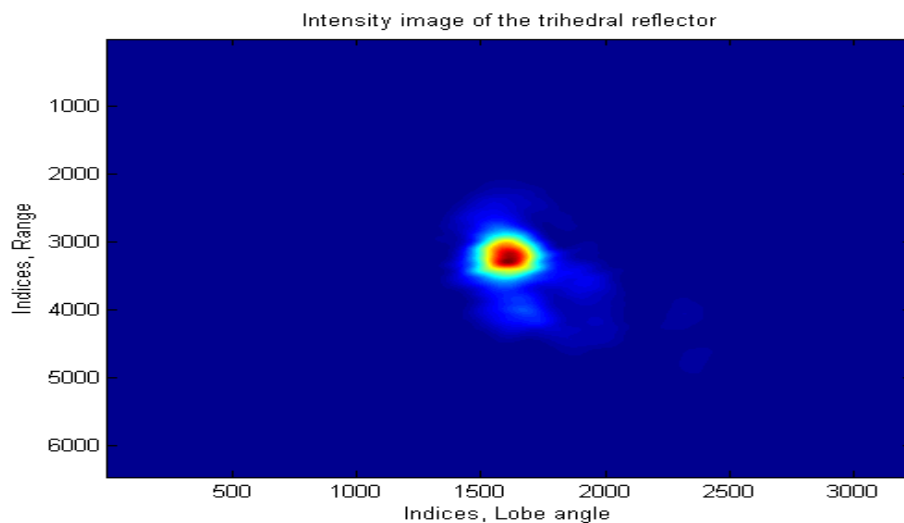


Figure 23 shows a close-up of the trihedral reflector in Figure 14. A 64×32 chip was extracted and interpolated 100 times by way of zero padding in the frequency domain. The maximum intensity value in this plot is used as a reference in Table 5 at the end of this section.

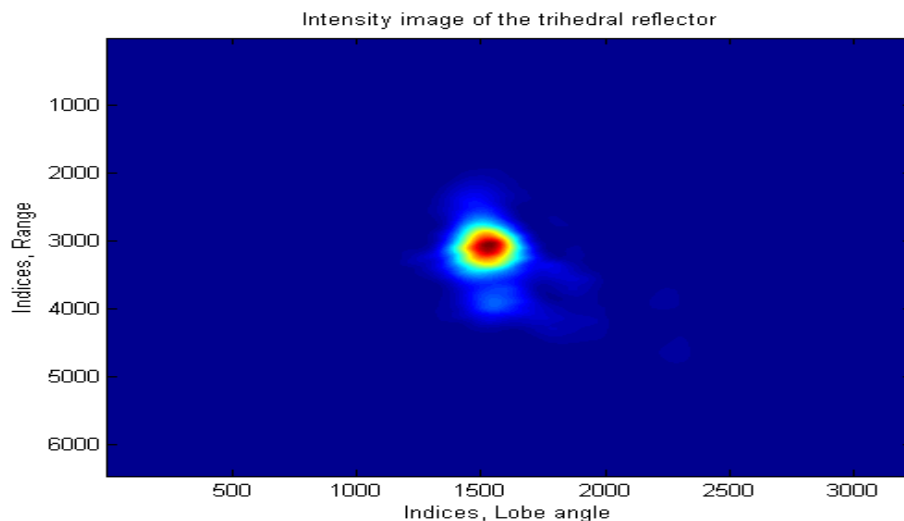


Figure 24 shows a close-up of the trihedral reflector in Figure 21. A 64×32 chip was extracted and interpolated 100 times by way of zero padding in the frequency domain. The relative (to the deterministic solution) maximum intensity value is found in Table 5 at the end of this section.

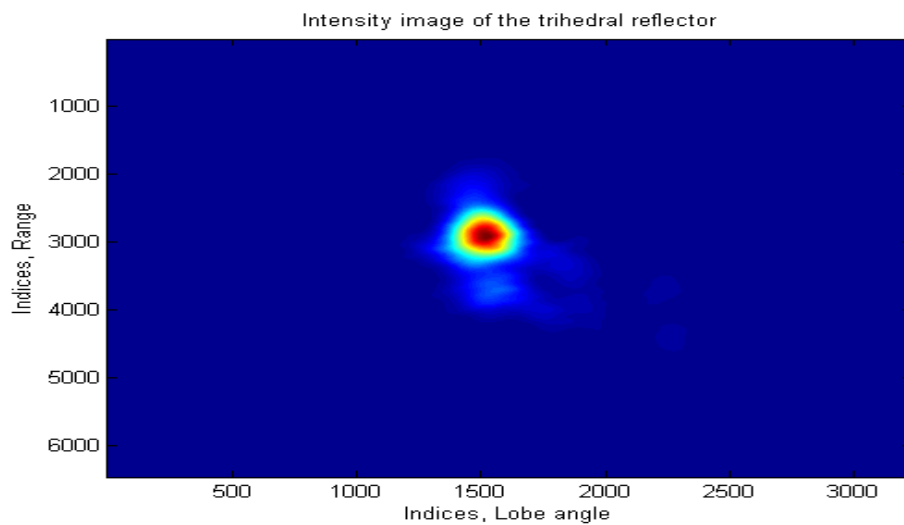


Figure 25 shows a close-up of the trihedral reflector in the image (not shown) corresponding to the deepest trough of the entropy plot. The interpolation strategy is the same as before. The relative (to the deterministic solution) maximum intensity value is found in Table 5 at the end of this section.

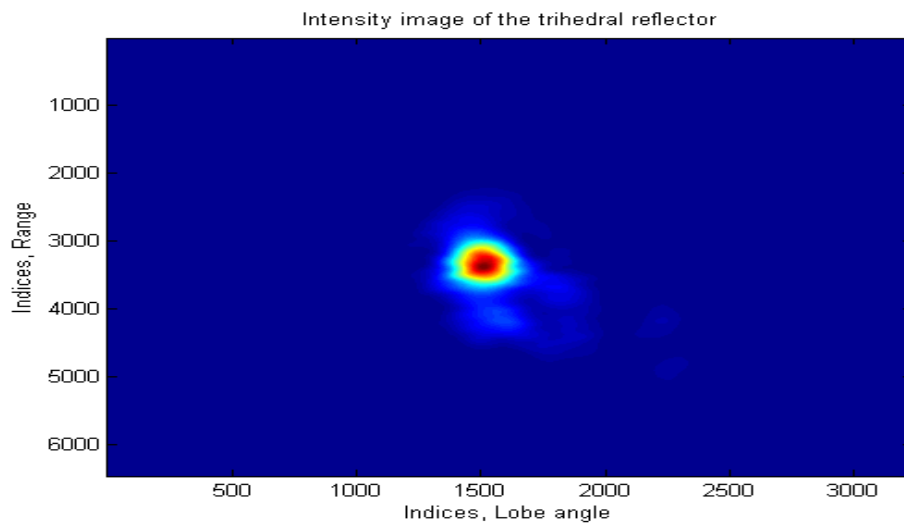


Figure 26 shows a close-up of the trihedral reflector in the image (not shown) corresponding to the highest peak of the maximum intensity plot. The interpolation strategy is the same as before. The relative (to the deterministic solution) maximum intensity value is found in Table 5 at the end of this section.

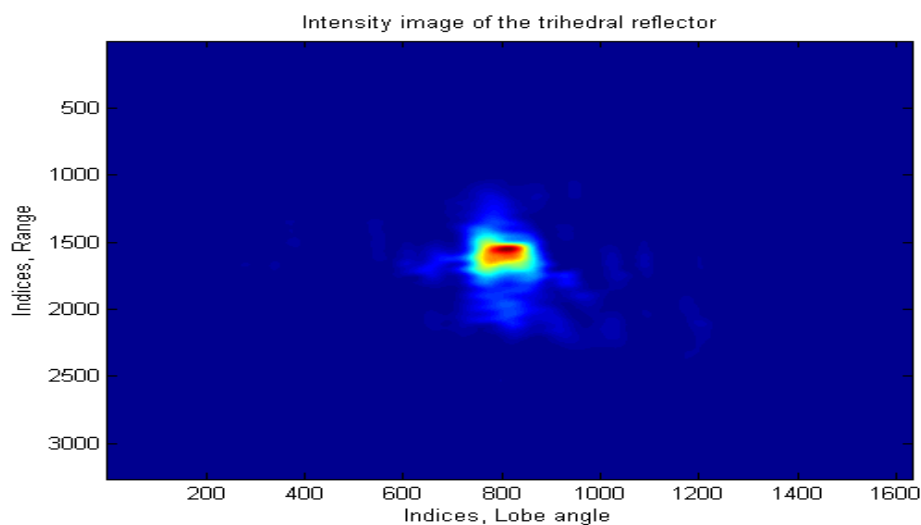


Figure 27 shows a close-up of the trihedral reflector in an image (not shown) corresponding to the highest peak of a correlation plot, obtained without up-sampling the data before varying the geometry. Notice that the mainlobe is very narrow and asymmetrical compared to the ones shown in previous plots.

Object function	$\Delta\zeta_p$ (rad)	$\Delta\zeta_z$ (rad)	Rel. max. I. (dB)
Correlation	-0.00235	-0.00415	-0.07580
Entropy	0.00265	0.00495	-0.22230
Maximum intensity	0.00200	0.00365	-0.00138

Table 5 resumes coordinates and relative maximum intensity values for auto-focused images. The scene in this case is Vidsel.

Object function	$\Delta\zeta_p$ (rad)	$\Delta\zeta_z$ (rad)	Rel. max. I. (dB)
Correlation	0.00055	0.00010	n/a
Entropy	-0.00160	-0.00430	n/a
Maximum intensity	0.00080	-0.00165	n/a

Table 6 resumes coordinates and relative maximum intensity values for auto-focused images. The scene in this case is Linköping.

5 Results - Revision B

MATLAB results for Revision B [10] will now be presented, along with some minor comments. The complete analysis is found in section 6.

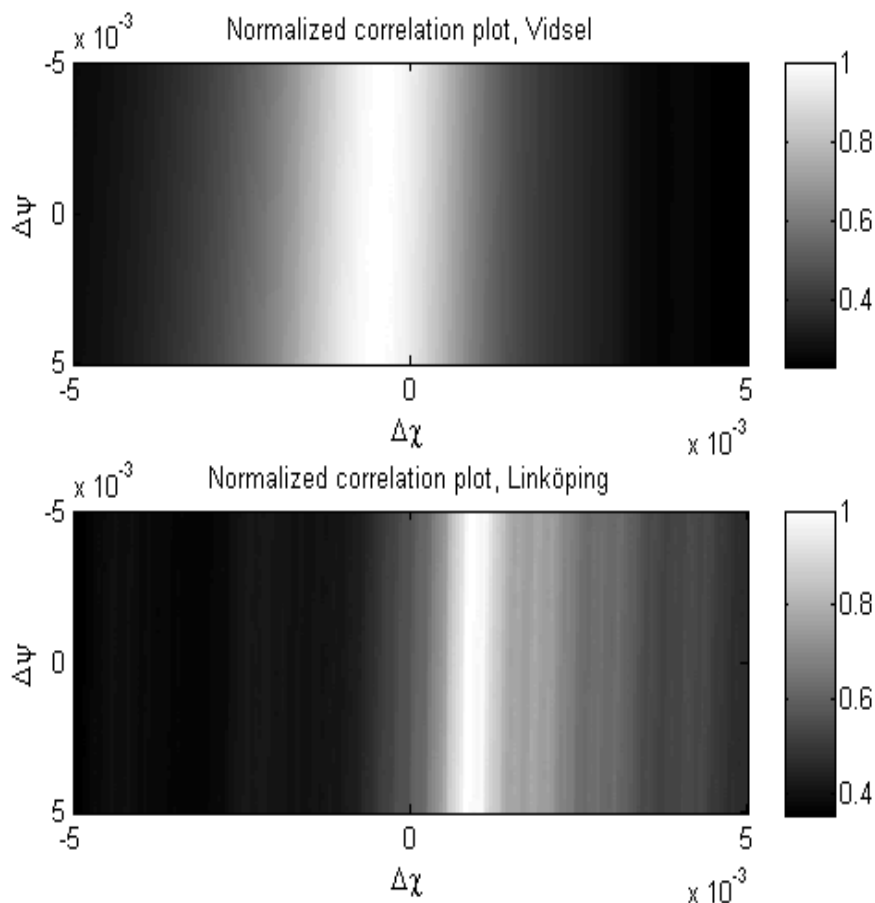


Figure 28 (Top) shows focus measures for Vidsel, while (Bottom) shows focus measures for Linköping. The object function is correlation. Measures corresponding to deterministic solutions are found at the centres of the plots. In other words, the axes display deviations from navigation data in differential variation quantities. The geometry is stepped $50 \mu\text{rad}$ in both dimensions. Before running the algorithm, the first data set was upsampled (additionally) by a factor four (in both range and cosine of sub-lobe angle) to improve the accuracy of the employed nearest neighbour interpolation and consequently the reflector result. This approach does not modify the general appearance of the correlation plot, although peaks and troughs may shift slightly along the ridge.

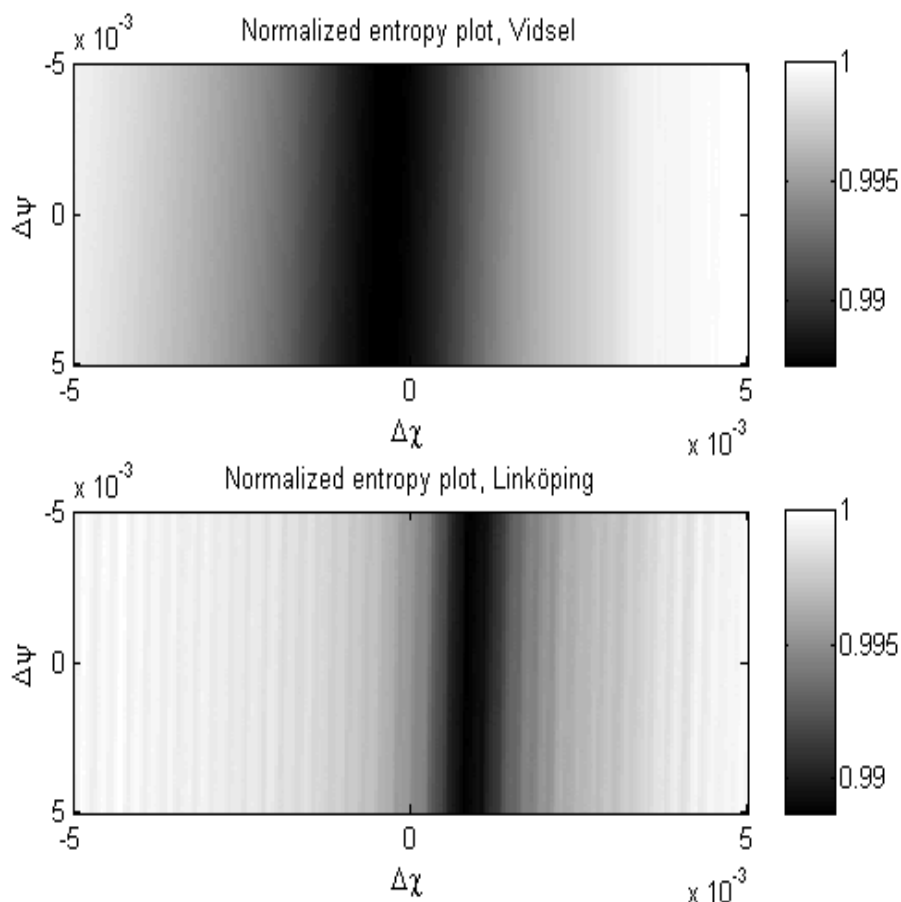


Figure 29 (Top) shows focus measures for Vidsel, while (Bottom) shows focus measures for Linköping. The object function is entropy. Measures corresponding to deterministic solutions are found at the centres of the plots. In other words, the axes display deviations from navigation data in differential variation quantities. The geometry is stepped $50 \mu\text{rad}$ in both dimensions. Before running the algorithm, the first data set was upsampled (additionally) by a factor four (in both range and cosine of sub-lobe angle) to improve the accuracy of the employed nearest neighbour interpolation and consequently the reflector result. This approach does not modify the general appearance of the entropy plot, although peaks and troughs may shift slightly along the ridge.

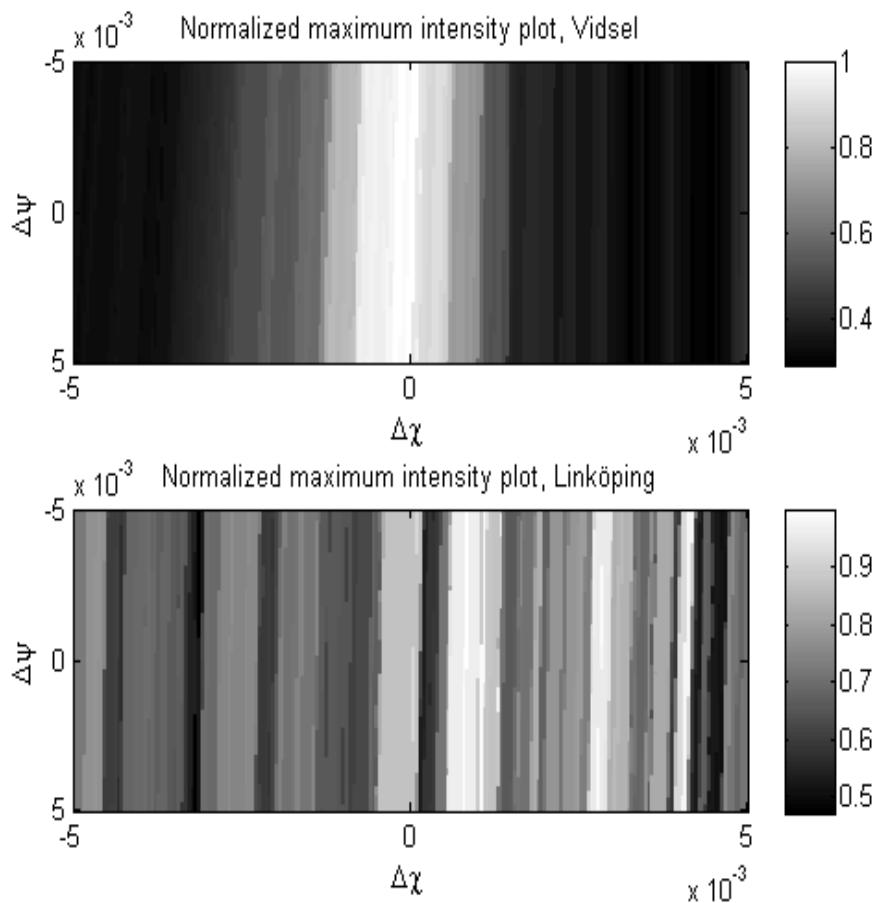


Figure 30 (Top) shows focus measures for Vidsel, while (Bottom) shows focus measures for Linköping. The object function is maximum intensity. Measures corresponding to deterministic solutions are found at the centres of the plots. In other words, the axes display deviations from navigation data in differential variation quantities. The geometry is stepped $50 \mu\text{rad}$ in both dimensions. Before running the algorithm, the first data set was upsampled (additionally) by a factor four (in both range and cosine of sub-lobe angle) to improve the accuracy of the employed nearest neighbour interpolation and consequently the reflector result. This approach does not modify the general appearance of the maximum intensity plot, although peaks and troughs may shift slightly along the ridge.

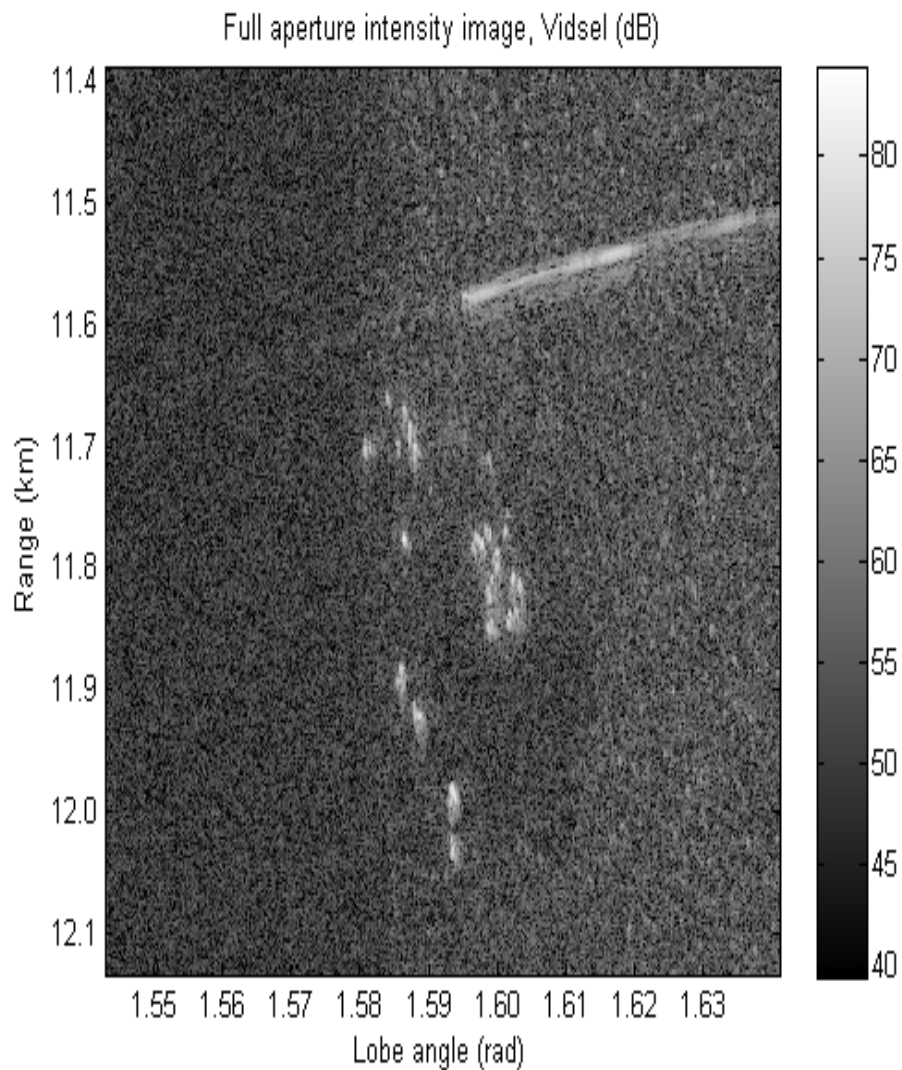


Figure 31 shows an autofocused intensity image of Vidsel. This image corresponds to the highest peak of the correlation plot and can be compared to the deterministically focused image in Figure 15. Note that similar (visually identical) results are acquired for the deepest trough of the entropy plot and the highest peak of the maximum intensity plot. Differential variation values for the peaks and the trough are summarized in Table 7 at the end of this section.

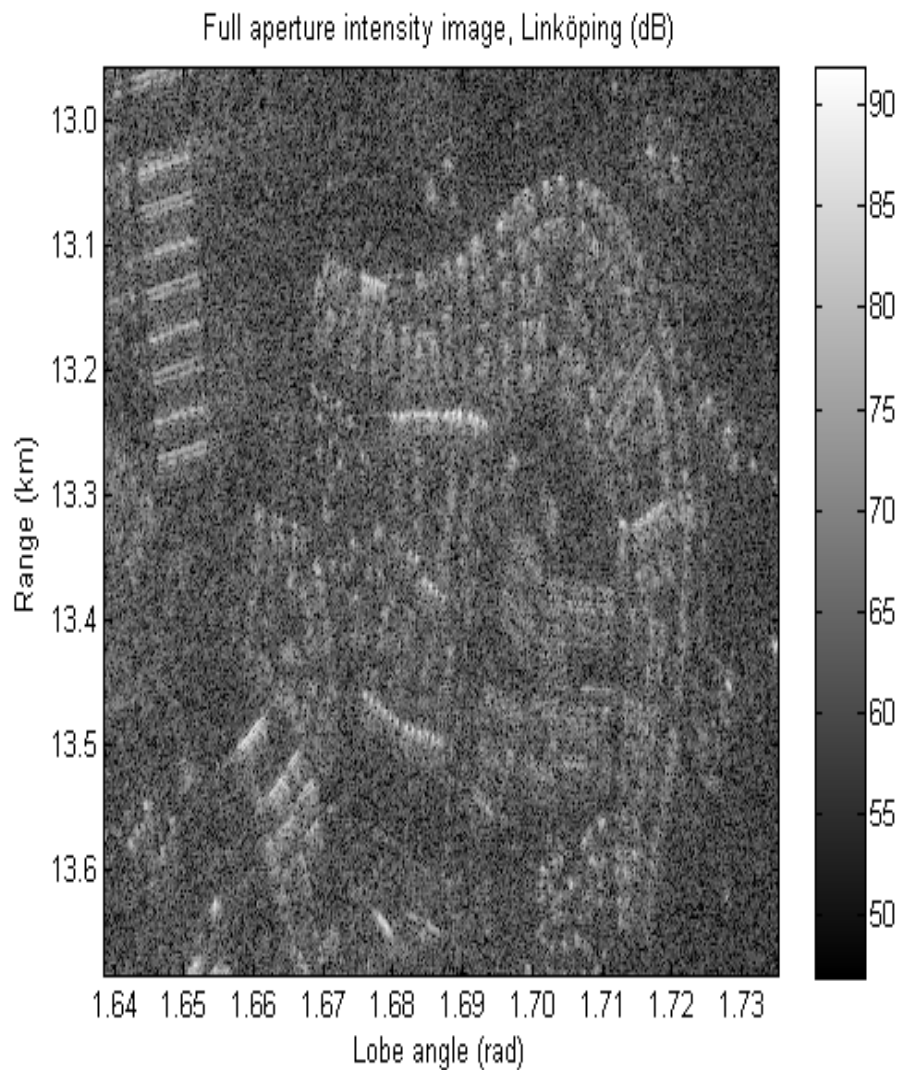


Figure 32 shows an autofocused intensity image of Linköping. This image corresponds to the highest peak of the correlation plot and can be compared to the deterministically focused image in Figure 17. Note that similar (visually identical) results are acquired for the deepest trough of the entropy plot and the highest peak of the maximum intensity plot. Differential variation values for the peaks and the trough are summarized in Table 8 at the end of this section.

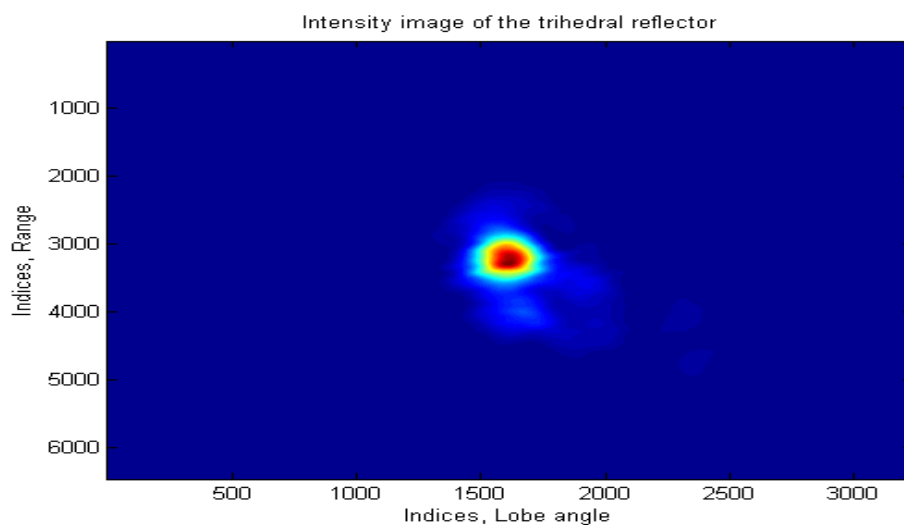


Figure 33 shows a close-up of the trihedral reflector in Figure 15. A 64×32 chip was extracted and interpolated 100 times by way of zero padding in the frequency domain. The maximum intensity value in this plot is used as a reference in Table 7 at the end of this section.

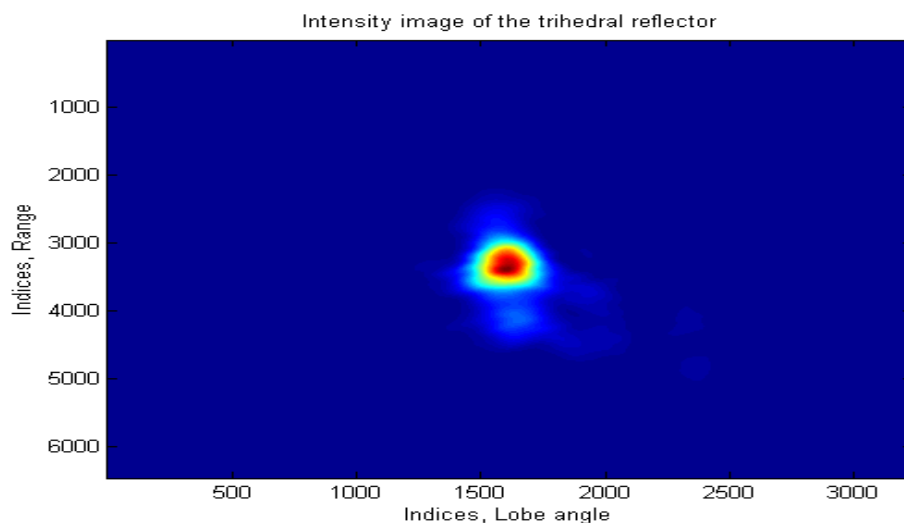


Figure 34 shows a close-up of the trihedral reflector in Figure 31. A 64×32 chip was extracted and interpolated 100 times by way of zero padding in the frequency domain. The relative (to the deterministic solution) maximum intensity value is found in Table 7 at the end of this section.

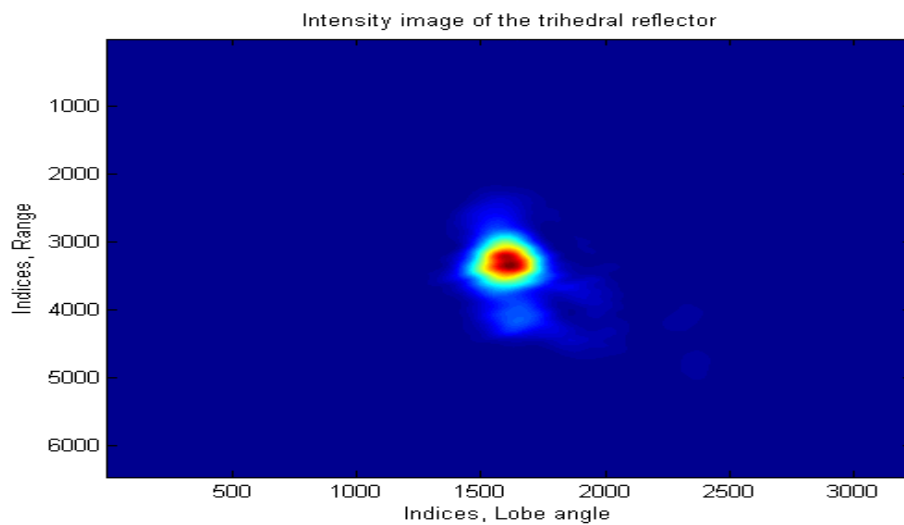


Figure 35 shows a close-up of the trihedral reflector in the image (not shown) corresponding to the deepest trough of the entropy plot. The interpolation strategy is the same as before. The relative (to the deterministic solution) maximum intensity value is found in Table 7 at the end of this section.

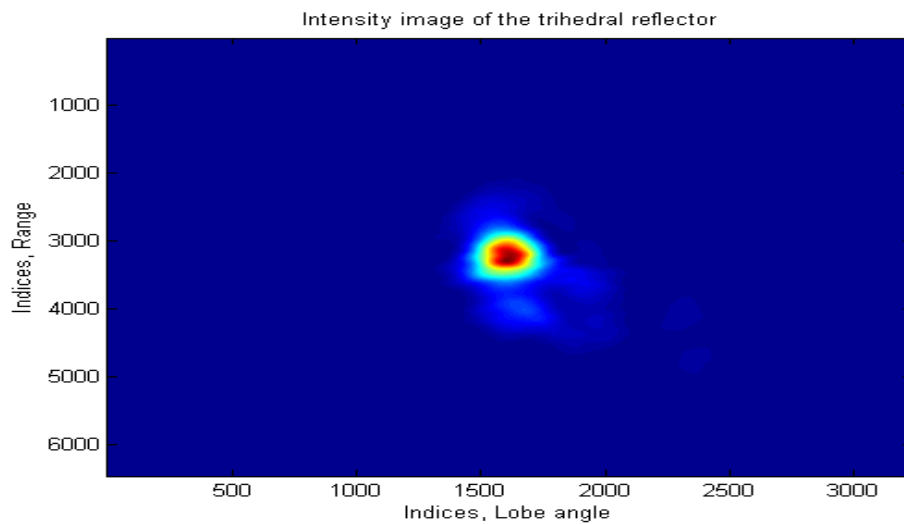


Figure 36 shows a close-up of the trihedral reflector in the image (not shown) corresponding to the highest peak of the maximum intensity plot. The interpolation strategy is the same as before. The relative (to the deterministic solution) maximum intensity value is found in Table 7 at the end of this section.

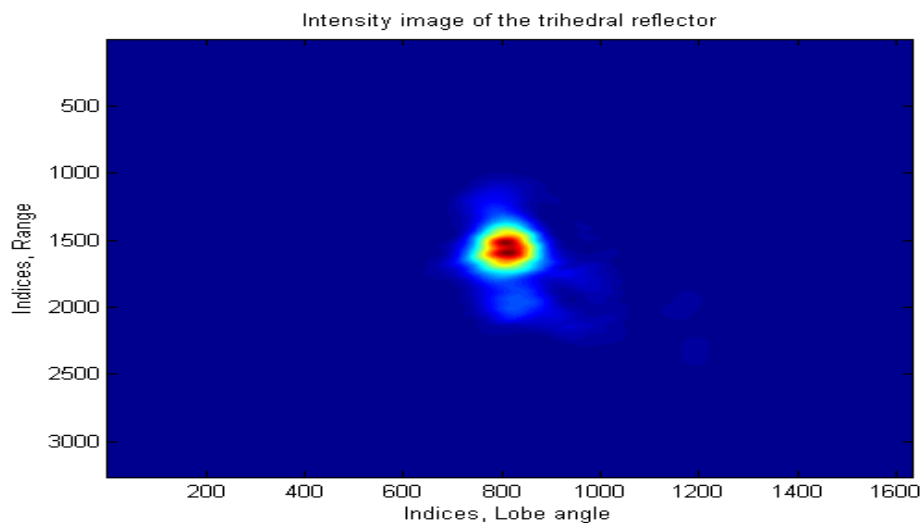


Figure 37 shows a close-up of the trihedral reflector in an image (not shown) corresponding to the highest peak of a correlation plot, obtained after up-sampling the data by factor two (in both range and cosine of sub-lobe angle). Notice that the mainlobe is split into two parts.

Object function	$\Delta\chi$ (rad)	$\Delta\psi$ (rad)	Rel. max. I. (dB)
Correlation	-0.00050	0.00375	-0.17608
Entropy	-0.00035	0.00240	-0.22944
Maximum intensity	0.00000	-0.00320	-0.02994

Table 7 resumes coordinates and relative maximum intensity values for auto-focused images. The scene in this case is Vidsel.

Object function	$\Delta\chi$ (rad)	$\Delta\psi$ (rad)	Rel. max. I. (dB)
Correlation	0.00090	0.00000	n/a
Entropy	0.00085	-0.00180	n/a
Maximum intensity	0.00085	0.00030	n/a

Table 8 resumes coordinates and relative maximum intensity values for auto-focused images. The scene in this case is Linköping.

6 Analysis

The joint analysis of the results will now be presented in three overlapping sub-sections: Object functions, Images and The trihedral reflector.

6.1 Object functions

Starting with Revision A, focus measure plots (see Figure 18–20) share the same pattern, namely a diagonal ridge (ridges for maximum intensity). However, characteristics of correlation are clear compared to characteristics of entropy and maximum intensity. Note for example that entropy ridges widen and deepen. Maximum intensity ridges are in turn rather rugged and increase in number with the intricacy of the scene, this is not favourable.

Focus measure plots for Revision B (see Figure 28–30) also share the same pattern, namely an orthogonal ridge (ridges for maximum intensity). Characteristics of correlation and entropy are fairly similar in this case, the limited swing of the variation quantities is a likely explanation for this. In other words, the sensitivity with respect to the independent parameters is different compared to Revision A. Statements concerning maximum intensity ridges in the previous paragraph apply to Revision B as well.

When searching for the best focus measure, Revision B has an apparent advantage over Revision A, specifically the potential of replacing one 2-dimensional search routine with two 1-dimensional search routines. This time saving approach is possible due to the orthogonality. Finally it should be pointed out, that in terms of computational efficiency, maximum intensity places first, followed in turn by correlation and entropy.

6.2 Images

A visual inspection of the images in Figure 14 and 21 and Figure 15 and 31 respectively, does not disclose any significant disparities. On one hand this implies that available navigation data is sufficiently accurate. On the other hand it implies that more than one geometry may produce a focused full aperture image. This assertion is motivated by the flight track figures found in Table 5 and 7, the deviations (giving the true images) from navigation data are large and more or less uncorrelated.

Note that these figures should be regarded as alternative navigation parameters (the figures in Table 6 and 8 should also be regarded as alternative) and not as true parameters. Thus, the autofocus algorithm cannot be used for tracking purposes (reference [21] deals with this subject in detail). An interesting observation in this context is, that focused images are acquired for all focus measures centred along the ridges. This leads to the query whether it is necessary to find the best focus measure or just the ridge?

A visual inspection of the images in Figure 16 and 22 and Figure 17 and 32 respectively, reveals that the autofocus algorithm sharpens blurry features. The reason for the loss of focus in the reference images, has afterwards been established to be faulty altitude information. Basically, the Focus Target Plane (FTP) was displaced by nearly 2 km, while processing. However, the algorithm compensates for this fact by finding an alternative geometry.

6.3 The trihedral reflector

The autofocused trihedrals in Figure 24–26 and Figure 34–36, look similar to the reference reflectors in Figure 23 and 33 respectively. This is positive, since the shape of point-like targets should be preserved.

Relative maximum intensity values (see Table 5 and 7) have decreased for all object functions and for both revisions. This should however not be over-interpreted, as the intensity in all cases have increased somewhere else (for other targets) in the image instead. It is a bit surprising though, that even the object function based on maximum intensity decrements the same measure after interpolation. Although, the decreases are very small and may arise due to sparse spacing of samples²³.

The effects illustrated in Figure 27 and 37 are more alarming. In the first example, the 3-dB width in the range dimensions is indeed finer than the theoretical resolution. In the second example, the mainlobe is split into two parts, substantial sidelobes have also been encountered. The effects disappear after additional upsampling of sub-image data. First and foremost, this calls for careful troubleshooting of the image formation stage. The object functions may also be mixed up in this quandary. High correlation for instance, is not a guarantee for a focused, uniform trihedral.

²³This is not related to the Nyquist-Shannon theorem, it merely suggests that sampling not necessarily pinpoints maxima.

7 Discussion & Conclusions

The report will now be concluded with a discussion divided into two subsections: Present status summarizes the current situation, while Future work surveys the upcoming development.

7.1 Present status

Both positive and negative results have been produced and presented. The sharpening of blurry features and the orthogonal relationship between the variation quantities (Revision B) promise well. Issues with the trihedral reflector are hopefully related to a minor flaw and not to the autofocus algorithm itself. The object functions however, still leave a great deal to desire, specifically when it comes to generating marked maxima/minima.

7.2 Future work

The algorithm development is still in an initial phase, with plenty of work ahead. Another revision is under review, leaving the ground plane approach behind in favour for the slant plane. Intuitively this seems like a wise decision, as the projection tends to complicate the processing. However, regardless of revision, there are a lot of things to look into. A suitable object function should for example be found. As has been shown, correlation, entropy and maximum intensity have disadvantages. An idea is to combine current functions in an attempt to extract the advantages. Other important examples of things to look into are listed below:

- When should the autofocus algorithm be activated?
- Are all variation quantities always essential?
- What is the relationship between the variation quantities (all four)?
- How large must the image(s) used for finding focus be?

Then there is the matter of processing time. The MATLAB results in this report have taken hours (days) to compile, despite the fact that two focusing dimensions have been disregarded.

A dedicated multi-core processor, running C or Assembler, is of course superior to a standard laptop with MATLAB installed among an abundance of other programs. However, at the moment it is hard to see this autofocus algorithm functioning in a real time environment.

A study regarding focus sensitivity with respect to the independent parameters will answer the first two questions in the list. Since there is an apparent connection to time consumption, this study should be prioritized.

The third question is harder to look into (it should however be addressed somehow), due to visualization issues (as well as extensive processing time).

The answer to the last question may finally be found in a trial and error fashion once the other queries are resolved.

Since this autofocus algorithm will not be fully functional in a near future, a concluding suggestion is to depart on a separate trail as well. For instance space variant processing with the PGA extensions described in [6].

8 References

- [1] L-E. Andersson. On the determination of a function from spherical averages. *Siam J. Math. Anal.*, 19(1):214–232, 1988.
- [2] C. Cafforio, C. Prati, and F. Rocca. SAR data focusing using seismic migration techniques. *IEEE Transactions on Aerospace and Electronic Systems*, 27(2):194–207, 1991.
- [3] W. G. Carrara, R. S. Goodman, and R. M. Majewski. *Spotlight Synthetic Aperture Radar: Signal Processing Algorithms*. Artech House Inc, Norwood, Ma, 1995.
- [4] I. G. Cumming and F. H. Wong. *Digital Processing of Synthetic Aperture Radar Data: Algorithms and Implementation*. Artech House Inc, Norwood, Ma, 2005.
- [5] P. Dammert and H. Hellsten. Adaptive SAR. Public Project Description 2/127 02-FCPM1040109 sv, SAAB EDS, 2010. Rev. F.
- [6] A. W. Doerry. Autofocus correction of SAR images exhibiting excessive residual migration. In *Proceedings of SPIE Radar Sensor Technology IX*, pages 34–45, 2005.
- [7] J. A. Fawcett. Inversion of N-dimensional spherical averages. *Siam J. Math. Anal.*, 45(2):336–341, 1985.
- [8] P-O. Fröling and L. M. H. Ulander. Evaluation of angular interpolation kernels in fast back-projection SAR processing. In *Proceedings of IEE Radar Sonar Navig.*, volume 153, 2006.
- [9] H. Hellsten. How to process SAR images when geometry parameters are unknown. Company Restricted Technical Report 14/0363-CSU 101 37 Uen, Ericsson Microwave Systems, 2006. Rev. A.
- [10] H. Hellsten. How to process SAR images when geometry parameters are unknown. Company Restricted Technical Report 7/0363-FCP 104 233, SAAB Microwave Systems, 2009. Rev. B.
- [11] H. Hellsten and L-E. Andersson. An inverse method for processing synthetic aperture radar data. *Inverse Problems*, 3:111–124, 1987.

-
- [12] H. Hellsten, P. Dammert, and A. Åhlander. Autofocus in fast factorized back-projection for processing of SAR images when geometry parameters are unknown. In *Proceedings of IEEE Radar Conference*, pages 603–608, Washington, DC, 2010.
- [13] H. Hellsten, L. M. H. Ulander, A. Gustavsson, and B. Larsson. Development of VHF CARABAS II SAR. In *Proceedings of SPIE Radar Sensor Technology*, pages 48–60, Orlando, FL, 1996.
- [14] C. V. Jakowatz, D. E. Wahl, P. H. Eichel, D. C. Ghiglia, and P. A. Thompson. *Spotlight-Mode Synthetic Aperture Radar: A Signal Processing Approach*. Kluwer Academic Publishers, 1996.
- [15] J. Kolman. PACE: an autofocus algorithm for SAR. In *Proc. of 1999 International Radar Conference*, pages 310–314, Virginia, USA, 2005.
- [16] J. McCorkle and M. Rofheart. An order $N^2 \log(N)$ backprojector algorithm for focusing wide-angle wide-bandwidth arbitrary-motion synthetic aperture radar. In *Proceedings of SPIE AeroSense Conference*, pages 25–36, Orlando, FL, 1996.
- [17] A. Moreira and Y. Huang. Airborne SAR processing of highly squinted data using a chirp scaling approach with integrated motion compensation. *IEEE Transactions on Geoscience and Remote Sensing*, 32(5):1029–1040, 1994.
- [18] R. L. Morrison, M. N. Do, and D. C. Munson. SAR image autofocus by sharpness optimization: a theoretical study. *IEEE Transactions on Image Processing*, 16(9):2309–2321, 2007.
- [19] J. G. Proakis and D. G. Manolakis. *Digital Signal Processing: Principles, Algorithms and Applications*. Pearson Prentice Hall, Upper Saddle River, New Jersey, fourth edition, 2007.
- [20] R. K. Raney, H. Runge, R. Bamler, I. G. Cumming, and F. H. Wong. Precision SAR processing using chirp scaling. *IEEE Transactions on Geoscience and Remote Sensing*, 32(4):786–799, 1994.
- [21] Z. Sjanic. Navigation and SAR auto-focusing in a sensor fusion framework. Licenciate Thesis ISSN 0280-7971, Linköping University, 2011.
- [22] R. J. Sullivan. *Radar Foundations for Imaging and Advanced Concepts*. SciTech Publishing Inc, Raleigh, NC, 2004.

- [23] L. M. H. Ulander, H. Hellsten, and G. Stenström. Synthetic-aperture radar processing using fast factorized back-projection. *IEEE Transactions on Aerospace and Electronic Systems*, 39(3):760–776, 2003.
- [24] A. Wyholt. SAR image focus errors due to incorrect geometrical positioning in fast factorized back-projection. Licenciate Thesis ISSN 1652-9103, Chalmers University of Technology, 2008.
- [25] L. Xi, L. Guosui, and J. Ni. Autofocusing of ISAR images based on entropy minimization. *IEEE Transactions on Aerospace and Electronic Systems*, 35(4):1240–1252, 1999.
- [26] A. F. Yegulalp. Fast backprojection algorithm for synthetic aperture radar. In *Proceedings of IEEE Radar Conference*, Waltham, MA, 1999.
- [27] A. F. Yegulalp. Minimum entropy SAR autofocus. In *ASAP '99 Workshop*, 1999.

I GBP - Algorithm realization

The equations below constitute the core of a discrete GBP realization²⁴.

$$R = \sqrt{(x_n - x_i)^2 + (y_n - y_i)^2 + (z_n - z_i)^2} \quad (1)$$

$$G(x_i, y_i) = \sum_{n=1}^N f(n, R) \cdot e^{\frac{j4\pi R}{\lambda}} \quad (2)$$

Received radar echoes $f(n, R_d)$ are assumed to be range compressed and demodulated to baseband, the total number of echoes equals N . Note that R_d represents range bins, while n represents track position indices.

Equation (1) calculates the slant range (R) between a pixel position with coordinates (x_i, y_i, z_i) and a track position with coordinates (x_n, y_n, z_n) .

The xy-plane (the ground plane) is chosen as the IDP, thus z_i is either a DEM level or some fixed nominal level, representable for the scene.

Equation (2) calculates the pixel value $G(x_i, y_i)$ for the image G .

Regard that R is a continuous variable as opposed to R_d . This implies that interpolation of $f(n, R_d)$ is a necessity to find $f(n, R)$.

The exponential function is the phase factor, with carrier wavelength λ .

²⁴This GBP formulation is valid for flight tracks along the x- or y-axis (nominally), in right- or left handed Cartesian coordinate systems (right- or left looking antennae).

II FFBP - Algorithm realization

The equation below constitutes the core of a discrete FFBP realization²⁵.

$$G(R_d, \theta_d) = G_1(R_1, \theta_1) \cdot e^{\frac{j4\pi(R_d - R_1)}{\lambda}} + G_2(R_2, \theta_2) \cdot e^{\frac{j4\pi(R_d - R_2)}{\lambda}} \quad (1)$$

Factorized radar echoes, $G_1(R_{d1}, \theta_{d1})$ and $G_2(R_{d2}, \theta_{d2})$, are assumed to be range compressed and demodulated to baseband. Note that R_{d1} and R_{d2} represent range bins, while θ_{d1} and θ_{d2} represent sub-lobe angles.

The slant plane is chosen as the IDP and the scene (the ground plane) is presumed to be located at some fixed nominal level.

Equation (1) calculates the pixel value $G(R_d, \theta_d)$ for the polar image G .

R_1, R_2, θ_1 and θ_2 are continuous variables as opposed to $R_{d1}, R_{d2}, \theta_{d1}$ and θ_{d2} . This implies that interpolation of factorized echoes is a necessity to find $G_1(R_1, \theta_1)$ and $G_2(R_2, \theta_2)$. See also Figure 1, section 2.2.2.

The exponential functions are phase factors, with carrier wavelength λ .

To compute R_1, R_2, θ_1 and θ_2 , the ground coordinates corresponding to R_d and θ_d must first be found. The next page summarizes a simple slant-to-ground conversion. Notations for the derivation are given below:

$\hat{\mathbf{u}}$ is the unit direction vector of the new sub-lobe (centre).

$\hat{\mathbf{q}}$ is the unit direction vector of the new sub-aperture.

\mathbf{p} are coordinates for the lobe-ground intersection.

\mathbf{o} are coordinates for the new sub-aperture centre.

R_d is the slant range and θ_d is the angle between $\hat{\mathbf{u}}$ and $\hat{\mathbf{q}}$.

²⁵This FFBP formulation is valid for flight tracks along the y-axis (nominally), in right- or left handed Cartesian coordinate systems (z-axis defined positive, right- or left looking antennae).

$$u_z = -(o_z - p_z)/R_d \quad (2)$$

$$\cos \theta_d = \hat{\mathbf{q}} \cdot \hat{\mathbf{u}} = q_x u_x + q_y u_y + q_z u_z \quad (3)$$

$$\kappa = \cos \theta_d - q_z u_z \quad (4)$$

$$q_y u_y = \kappa - q_x u_x \quad (5)$$

$$q_y^2 u_y^2 = \kappa^2 - 2\kappa \cdot q_x u_x + q_x^2 u_x^2 \quad (6)$$

$$u_y^2 = 1 - u_x^2 - u_z^2 \quad (7)$$

$$q_y^2(1 - u_x^2 - u_z^2) = \kappa^2 - 2\kappa \cdot q_x u_x + q_x^2 u_x^2 \quad (8)$$

$$K = \kappa^2 - q_y^2 + q_y^2 u_z^2 \quad (9)$$

$$(q_y^2 + q_x^2)u_x^2 - (2\kappa \cdot q_x)u_x + K = 0 \quad (10)$$

$$u_y = \pm \sqrt{1 - u_x^2 - u_z^2} \quad (11)$$

$$\mathbf{p} = \hat{\mathbf{u}} \cdot R_d + \mathbf{o} \quad (12)$$

Equation (10) is quadratic, giving one solution for right looking antennae and one for left looking antennae.

Equation (11) determines if the lobe is squinted back or forth with respect to the nominal broadside direction.

The following equations compute R_1 , R_2 , θ_1 and θ_2 :

$$R_1 = \|(\mathbf{p} - \mathbf{o}_1)\| \quad (13)$$

$$R_2 = \|(\mathbf{p} - \mathbf{o}_2)\| \quad (14)$$

$$\theta_1 = \arccos\left(\frac{\hat{\mathbf{q}}_1 \cdot (\mathbf{p} - \mathbf{o}_1)}{R_1}\right) \quad (15)$$

$$\theta_2 = \arccos\left(\frac{\hat{\mathbf{q}}_2 \cdot (\mathbf{p} - \mathbf{o}_2)}{R_2}\right) \quad (16)$$

$\hat{\mathbf{q}}_1/\hat{\mathbf{q}}_2$ are unit direction vectors of preceding sub-apertures.

$\mathbf{o}_1/\mathbf{o}_2$ are coordinates for preceding sub-aperture centres.